



DROP-IT

DELIVERABLE 3.2

Solar cells with PCE > 12% based on inkjet-printed B-LFPs (areas 0.04-1 cm²)

Due date of deliverable: 2021/10/31

Actual submission date: 2021/11/30

Deliverable number: D3.2
Due date: 31.10.2021
Nature¹: R
Dissemination Level¹: PU
Work Package: WP3
Lead Beneficiary: SAULE
Contributing Beneficiaries: SRI, UJI

¹ **Nature:** R = Report, P = Prototype, D = Demonstrator, O = Other

Dissemination level PU = Public PP = Restricted to other programme participants (including the Commission Services) RE = Restricted to a group specified by the consortium (including the Commission Services) CO = Confidential, only for members of the consortium (including the Commission Services) Restraint UE = Classified with the classification level "Restraint UE" according to Commission Decision 2001/844 and amendments Confidential UE = Classified with the mention of the classification level "Confidential UE" according to Commission Decision 2001/844 and amendments Secret UE = Classified with the mention of the classification level "Secret UE" according to Commission Decision 2001/844 and amendments





DOCUMENT HISTORY

<i>Version</i>	<i>Date</i>	<i>Reason of change</i>
1	2021/10/20	SAULE contribution
2	2021/10/28	SRI contribution
3	2021/11/30	Revised by UVEG – necessary to be updated as soon as inkjet printer will be running in inert atmosphere (glove box).
4	2022/06/17	Revised by Saule – inkjet printing section added, table of B-LFPs/G-LFP added.





Table of Content

1	INTRODUCTION	4
1.1	INKJET PRINTING AND FILM QUALITY	4
1.2	LFPs SOLAR CELL DESIGN	7
1.3	SHORT REVIEW: STATE-OF-THE-ART AND CHALLENGES OF SN-BASED PEROVSKITE SOLAR CELLS	8
2	DESCRIPTION OF WORK & MAIN ACHIEVEMENTS	12
2.1	FABRICATION OF SPIN-COATING TIN-BASED (SP-LFP) SOLAR CELLS	12
2.1.1	Preparation of the LFP precursor solution	12
2.1.2	Assembly of SP-LFP devices	12
2.1.3	Characterization of SP-LFP films and devices	13
2.2	FABRICATION OF TIN-BASED B-LFPs SOLAR CELLS	14
2.2.1	Ink preparation	14
2.2.2	Device assembly	14
2.2.3	IV Characterization	15
2.2.4	Passivation strategies for improved stability	15
2.2.5	Tests with alternative ETMs	15
3	RESULTS	15
3.1	SP-LFP FILMS AND DEVICES	15
3.1.1	Morphological and structural characterization of SP-LFP	15
3.1.2	Optical characterization of the SP-LFP films	16
3.1.3	Characterization of the SP-LFP devices under 1-sun illumination	17
3.2	BLADE COATED TIN-BASED PEROVSKITE SOLAR CELLS UNDER 1 SUN ILLUMINATION	19
3.3	BLADE COATED TIN-BASED PEROVSKITE SOLAR CELLS UNDER LOW LIGHT CONDITIONS	22
3.4	PASSIVATION STRATEGIES FOR IMPROVED STABILITY	23
3.5	TESTS WITH ALTERNATIVE ETMS	23
3.6	INKJET-PRINTED TIN-BASED PEROVSKITE	24
3.6.1	Print quality tests	24
3.6.2	Inkjet-printed tin-based perovskite solar cells under 1 sun illumination	42
4	DEVIATIONS FROM THE WORKPLAN	43
5	CONCLUSIONS & FUTURE DIRECTIONS	43
6	REFERENCES	45
7	ANNEX	46





1 Introduction

This deliverable reports on the fabrication of lead-free perovskite solar cells for benchmarking purposes (B-LFPs), manufactured on rigid substrates through spin-coating and on flexible substrates through blade coating and inkjet printing, respectively, for potential large scale and industrial production. Photovoltaic devices based on polycrystalline and nanoparticulate B-LFP films will serve as reference (efficiency and stability) for future novel generations of Lead-Free Perovskites (G-LFPs) devices developed in DROP-IT. In the project we have concentrated on FASnI_3 LFPs for benchmark solar cells and we will focus on different tin-based Ruddlesden-Popper phases (high-n and 2D-3D assemblies) as G-LFPs, as summarized in Table A1 (Annex 1).

As a standard, solar cells with active areas in the range of $0.04 - 1 \text{ cm}^2$ were fabricated and their current-voltage properties (IV-curve) were characterized under 1-sun and low-light conditions.

1.1 Inkjet printing and film quality

Drop-on-demand digital inkjet printing is a mature, reliable, versatile, and cost-efficient technology that evolved over the last decades and has demonstrated its importance far beyond classical visualization applications, especially in the field of printed electronics. The additive nature of the printing process, the wide range of materials that can be formulated as inks, and the ability to address different production scales, from prototypes to high volume, along with minimal material waste, are some of the critical factors that enable the use of printing processes in electronics manufacturing and many other areas. Inkjet printing can be classified as a non-contact method.

The interaction of the applied ink and the substrate plays a vital role in the quality of the resulting film. The properties of the ink and the substrate must be complementary and well-matched, to improve adhesion and avoid repelling as well as uncontrolled spreading. An array of nozzles is used to draw and deposit tiny droplets of the perovskite ink onto a flat substrate to yield a thin film with a predefined pattern. The most important parameters that influence the quality of the printed films are the printing speed, droplet (size, shape, velocity), the waveform (dependent on nozzle dimension), ink rheology and surface tension, and the drop trajectory. Because this technique is based on the ejection of droplets that, once deposited on the substrate, merge together thanks to their adhesive forces; in the case of piezoelectric jetting (figure 5), a voltage is applied to an actuator that releases ink through oscillating bending.

This technique is based on the ejection of droplets that, once deposited on the substrate, merge together thanks to their adhesive forces; in the case of piezoelectric jetting (figure 1), a voltage is applied to an actuator that releases ink through oscillating bending. The motion of this piezoelectric actuator is linked to the profile of the applied voltage over time, or waveform, which directly dictates the droplet formation process.

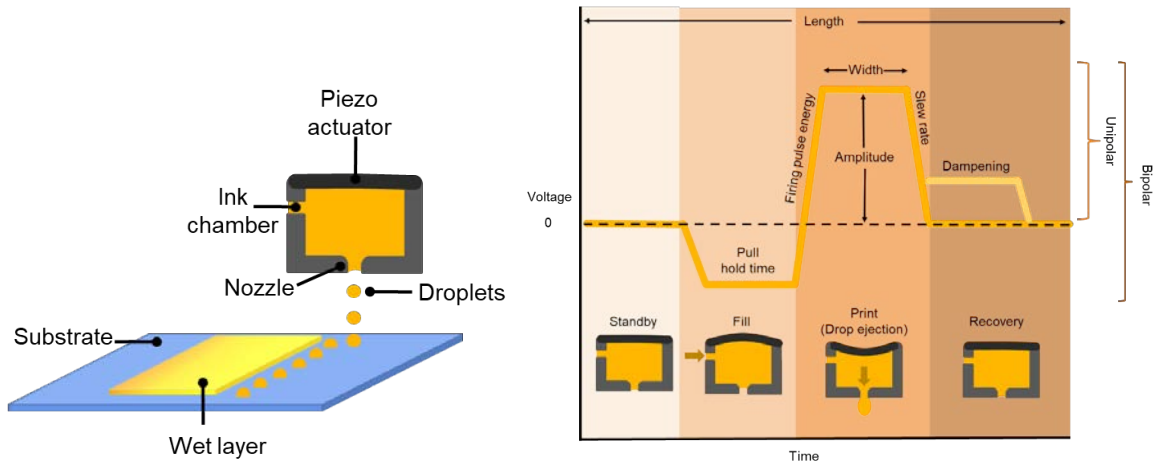
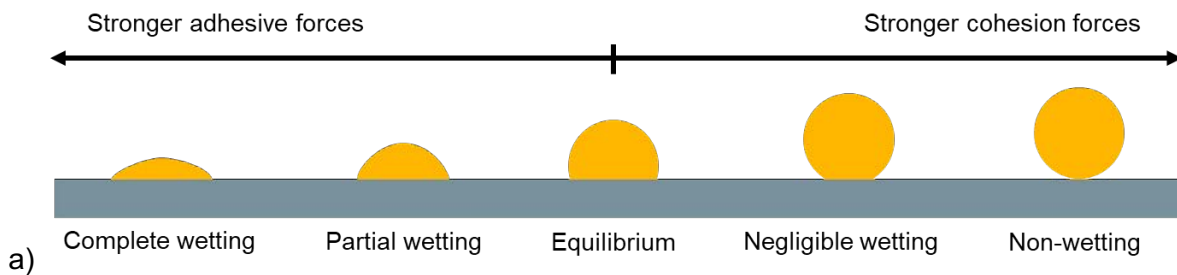


Figure 1. Principles of inkjet printing and jetting waveforms.

Besides the jetting stability, the quality of the printed layer is also dependent on processes that occur during the liquid layer formation like wetting, spreading/levelling, and evaporation that happen before the annealing of the film (figure 2). The drop-substrate interaction is determined by the balance between the surface tension of the liquid (cohesive forces) and the surface energy of the substrate (adhesive forces), as well as its roughness. Comparably, the spreading and coalescence of individual droplets into a uniform liquid later depends on the rheological properties of the ink and the interactions at the interface; high viscosity, significant dewetting and diffusion flows can contribute to a thickness gradient of the final layer. During the transformation to the solid perovskite phase the wet film contracts, usually with pinned contact lines at the edges, where the drying is faster since there is less liquid to evaporate; at this time four forces are simultaneously in action: capillary levelling of the liquid film surface, lateral solute diffusion, solvent evaporation, and Marangoni drag from solute concentration gradients. As a result, material tends to accumulate at the edges of the shrinking film, leaving a morphology with a low number of particles at the centre, known as the coffee ring effect.



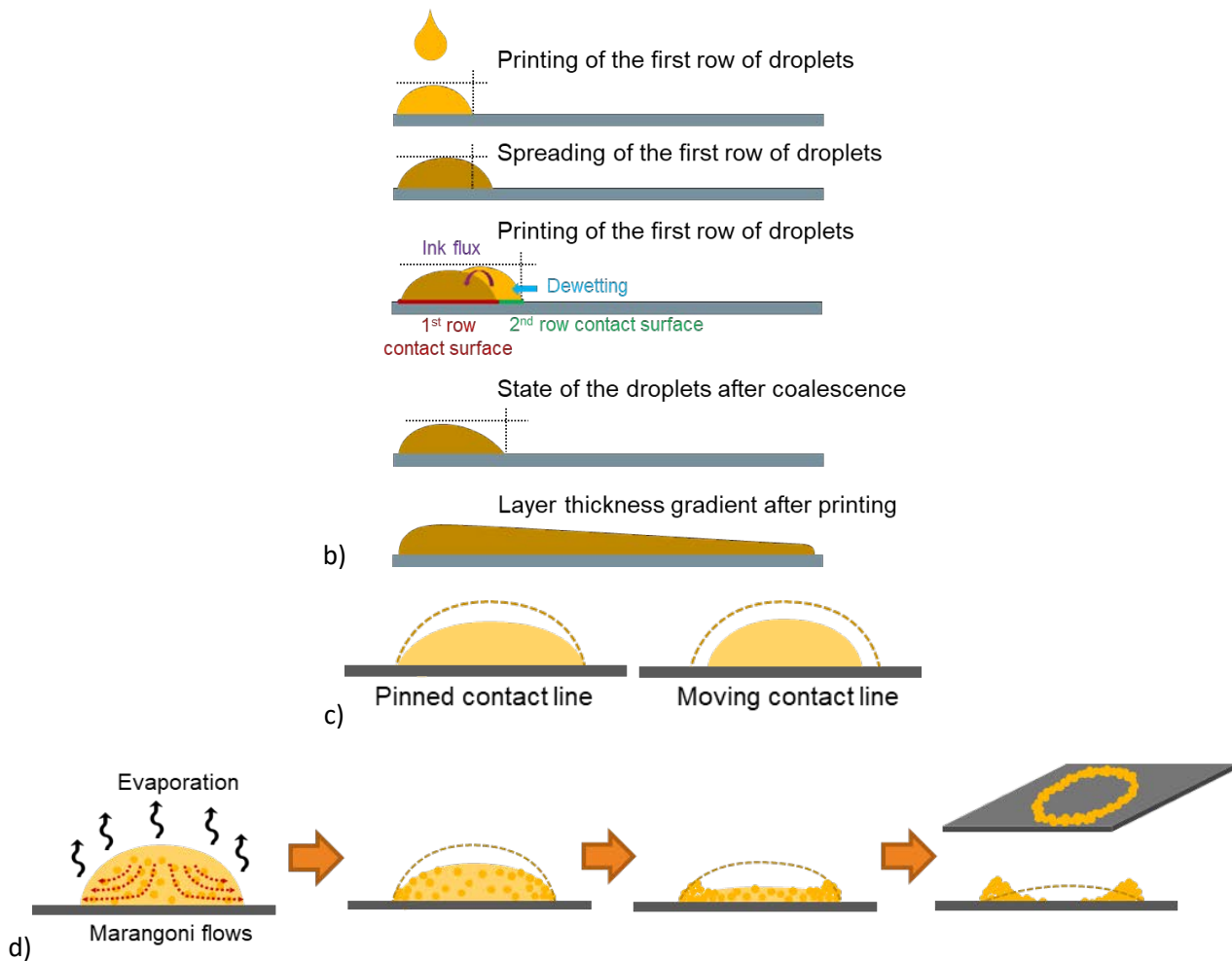


Figure 2. Liquid film processes a) ink-substrate wetting b) droplet spreading and coalescence c) droplet drying modes d) coffee ring formation during drying.

Once the layer dries, the quality of the print can be assessed by the connectivity and edge sharpness achieved at each row of droplets (figure 3), and therefore decide if the employed drop spacing/resolution was good enough for the application. If the spacing between drops is too large the resulting pattern becomes disconnected, but if they are too close it can lead to accumulation of liquid and bulging spots; another factor to consider is temperature, colder conditions limit the spreading of merged droplets and induce wavy lines, while if the substrate is too hot, the evaporation happens too quickly and produce non uniform stacking marks along the path.

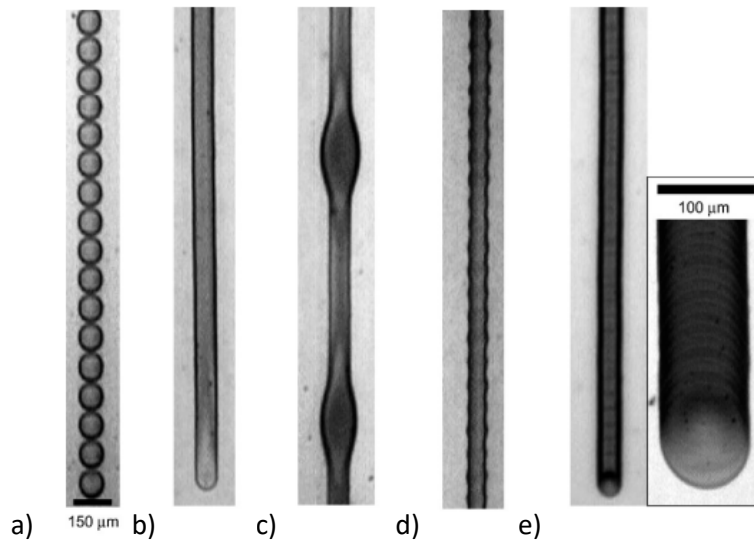


Figure 3. Behaviour of inkjet-printed lines:

- a) disconnected b) uniform c) bulging d) scalloped e) stacked coins pattern.

1.2 LFPs solar cell design

The device architecture of perovskite solar cells is composed of several stacking films (figure 4); at the base a transparent conductive oxide is placed above the substrate and on the top a metal contact usually closes the electrical circuit. The charge separation and transport are handled by middle layers of electron transporting materials (ETM) and hole transporting materials (HTM), which are mediated by the perovskite absorber layer; the configuration of these inner layers can be either n-i-p or inverted p-i-n, the cells can also be labelled mesoporous or planar depending on the properties of the ETM film.

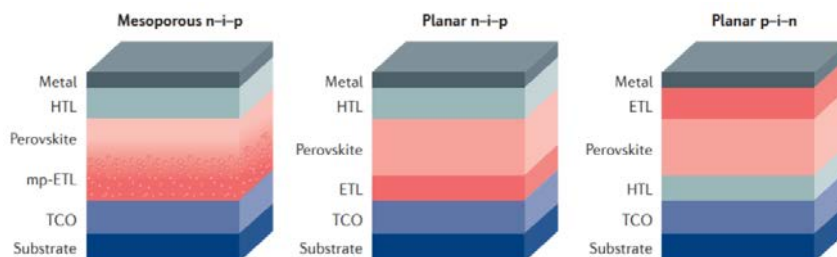


Figure 4. Typical architectures for perovskite solar cells.^[1]

For tin perovskites p-i-n devices are commonly found in the state of the art, and several HTMs and ETMs have been successfully integrated (figure 5). The key factors for good efficiencies are matching of energy levels to ensure proper charge transport dynamics and good interface contact to minimize internal resistance.

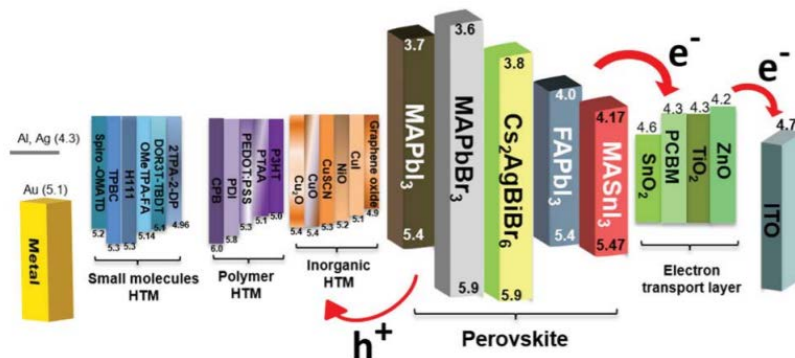


Figure 5. Examples of typical materials employed for perovskite solar cell fabrication.^[2]

The design implemented in this report is directly based on the achievements of WP2-3; deliverable 2.1 proved that PET is a commercially available flexible substrate with attractive properties, such as resistance to physical and thermal processes without loss of transparency, relatively lower cost, and most importantly a good printability of LFP inks. In D2.2 PEDOT:PSS was shown to be compatible with large-scale processing and exhibited good morphological, structural, optical and electrical properties; in D2.3-2.5 and D3.1 tin-based (FASnI₃) inks were found to be the most successful for the deposition of pinhole-free, homogeneous and reproducible perovskite layers.

Concurrently, a systematic study focused on developing solar cells through spin-coating of the LFP (SP-LFP) precursor solutions on rigid substrates (ITO glass) has been carried out as benchmark and to test device configurations and film additives to be implemented later in inkjet printing; a detailed analysis of the efficiency performance and long-term stability achievements is provided in this document. These results provide new insights onto the LFP device's functioning and will serve as a solid cornerstone for benchmarking purposes of the devices based on printing methodologies.

1.3 Short review: state-of-the-art and challenges of Sn-based perovskite solar cells

Organic-inorganic metal halide perovskites have unique optical and electrical properties, which make them an excellent class of materials for a broad spectrum of optoelectronic applications, including photovoltaic applications. High power conversion efficiency was achieved with Pb-based compositions which are toxic to the environment and a potential health hazard to animals and humans. Sn-based perovskite compositions are considered as most promising alternatives due to bandgap values close to the optimum for solar cells, strong absorption profile – very similar to the Pb-based counterparts–, and sufficient charge carrier mobility.

However, Sn-based perovskites suffer from low defect tolerance driven by fast crystallization, oxidative instability of Sn²⁺ (converting into Sn⁴⁺) and the essential necessity for processing in strictly controlled environmental conditions (inert gas e.g., N₂ or Ar, with O₂ and H₂O levels 0.1 ppm). In fact, Sn-based perovskite films do not even form the perovskite phase when processed and annealed in ambient environment!

Although tormented by a lower stability compared to Pb²⁺, Bi³⁺ or Sb³⁺, Sn²⁺ is the most promising candidate to substitute the toxic lead compound owing to excellent optical and electrical properties, especially suitable for solar cell applications. Sn-based perovskites with an optical bandgap in the range of 1.2–1.4 eV could theoretically reach a power conversion efficiency of ca. 33.16% according to the Shockley-Queisser detailed balance limit.^[3] Despite possessing similar optoelectronic features as the Pb-based perovskite counterparts, Sn-based perovskite solar cells reached significantly lower

record efficiency of 14.81% compared to the 25.7% of Pb-based compounds (on rigid glass substrates).^[4,5] This gap originates from the low stability of Sn-based perovskites, the instability of the 2+ oxidation number and thus the rapid oxidation of Sn²⁺ to Sn⁴⁺, leading to high dopant concentrations and limiting the efficiency and reproducibility of the solar cell. In addition, compact and pinhole-free films are difficult to obtain. Sn-based perovskite thin films typically show poor crystalline quality and rough morphologies with much smaller grains in comparison to Pb-based perovskite films.

The main challenges and opportunities in the field of Sn-based perovskite photovoltaics are illustrated in figure 5 and summarized below:

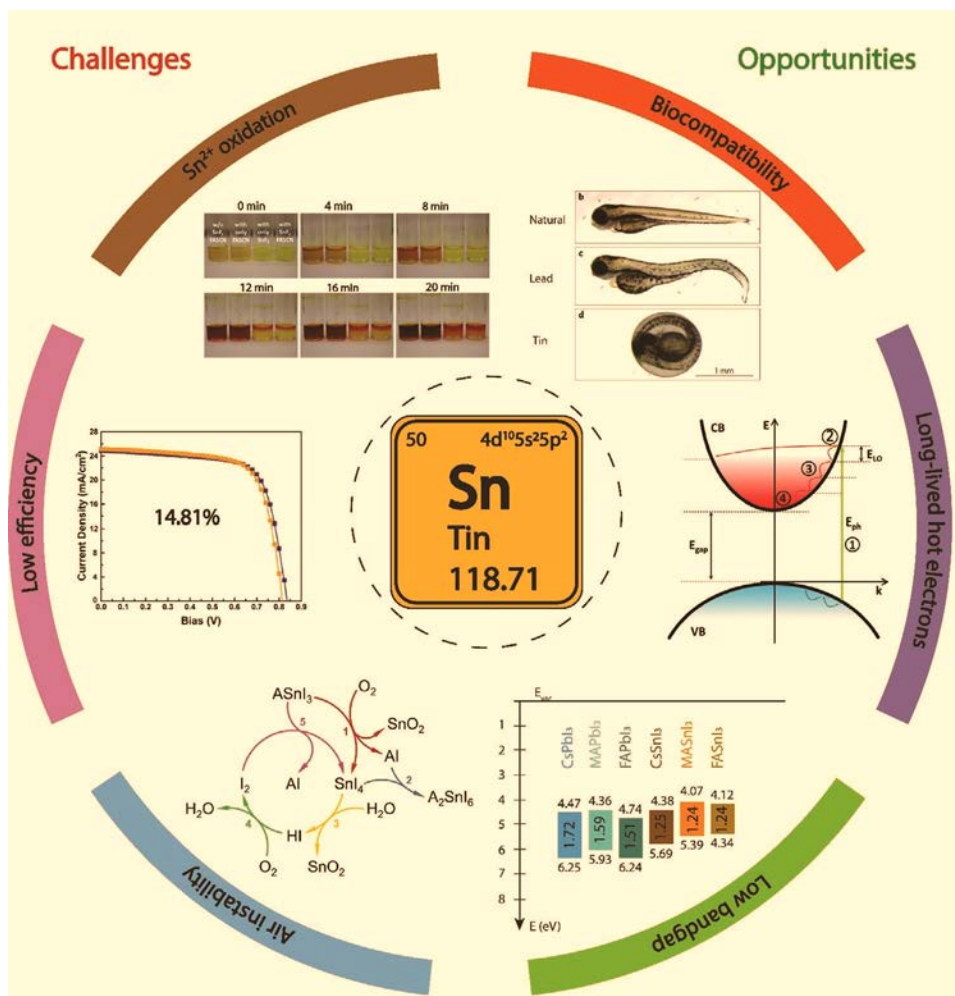


Figure 5. Summary of the opportunities and challenges for Sn-based tin perovskite materials.^[6]

Challenges:

- Sn²⁺ to Sn⁴⁺ oxidation
- Low power conversion efficiency
- Air instability

Opportunities:

- Biocompatibility
- Long lived hot electrons
- Low bandgap

The crystallization dynamics are critical for the formation of high-quality Sn-based perovskite thin films. Anisotropic nucleation and growth due to faster crystallization is observed in Sn-based thin films in comparison to Pb-based thin films. A fast crystallization process is more likely to produce structural defects such as vacancies, pinholes, as well as orientation and stacking disorder of the grains. These structural defects cause an increase in nonradiative recombination and determine short circuits and low open-circuit voltages in solar cells. The key to realize high quality tin perovskite films is through the control of the fast crystallization process. Systematic studies on the crystallization mechanism of Sn-based perovskites thin film are scarcely reported, due to the difficulty in studying their intrinsic properties driven by the facile oxidation of Sn^{2+} .

The strategies that have been used to obtain efficient Sn-based solar cells are more complex, since ink stability, processing techniques, and processing environment must be thoroughly considered and strictly controlled. The most important strategies (figure 6) are i) reducing agents to control the oxidation state of the Sn-cation, ii) chemical composition on A and X sites of the ABX_3 structure, iii) bulk and surface passivation, iv) modification of the perovskite composition (Dion-Jacobsen or Ruddlesden-Popper-phases) and v) 2D/3D perovskite mixtures.

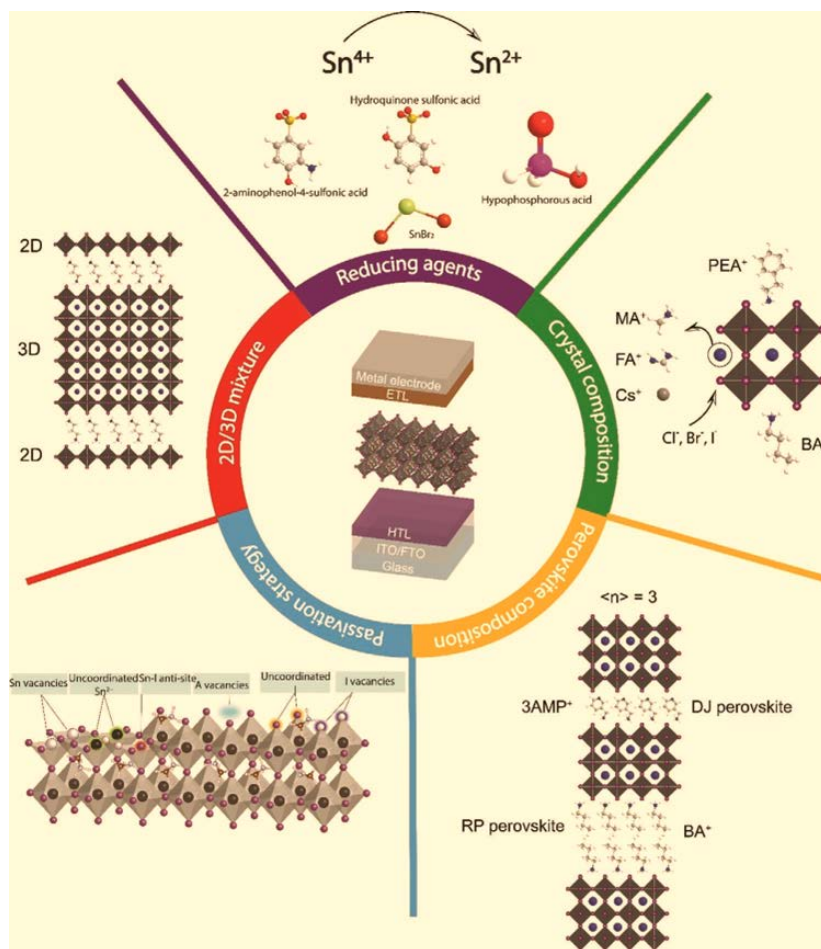


Figure 6. Summary of the opportunities and challenges for Sn-based tin perovskite materials.^[6]



High quality Sn-perovskite thin films leading to record efficiencies have been reported exclusively by anti-solvent quenching of spin-coated perovskite layers. Mimicking the anti-solvent quenching effect for Sn-perovskites films deposited by large scale deposition methods such as blade coating or inkjet has been proven to be challenging. To the best of our knowledge there are no reports on blade coated Sn-perovskite solar cells. The best performing inkjet printed Sn-based perovskite solar cells on glass substrates were reported in 2020 by He et al. [7] The authors claimed to achieve anti-solvent-free spin-coated (PCE 8.9%) as well as inkjet-printed (PCE 5.5%) FASnI_3 champion devices by combining preformed perovskite crystals with a vacuum treatment of the deposited wet film. However, those reported PCE values could not be reproduced or improved by the community till date.



2 Description of work & main achievements

2.1 Fabrication of spin-coating tin-based (SP-LFP) solar cells

The study was focused on the deposition of LFPs through spin-coating for the fabrication of tin-based solar cells (figure 7), to assess the optimum performances and long-term stabilities that can be achieved in our laboratories, as the best performing tin-based devices are reported to be obtained by spin-coating procedures. A series of additives (NaBH_4 , Dipl and their combination) were systematically incorporated into the precursor solutions for an exhaustive study of their impact on the device's performance.

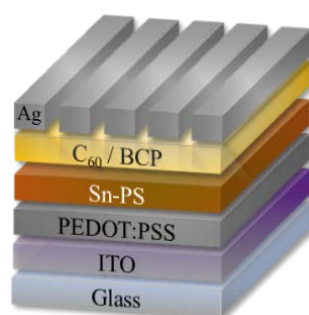


Figure 7. Architecture of the Sn-based LFP devices fabricated through spin-coating.

2.1.1 Preparation of the LFP precursor solution

Tin(II) iodide (SnI_2 , 99.99%), tin(II) fluoride (SnF_2 , 99%), Bathocuproine (BCP, 99.99%), N,N-dimethylformamide (DMF, 99.8%), NaBH_4 and dimethylsulfoxide (DMSO, 99.8%) were purchased from Sigma-aldrich. PEDOT:PSS A14083 aqueous solution was purchased from Heraeus. C_{60} (99.95%) was obtained from Nano-C. Formamidinium iodide (FAI, 99.99%) was purchased from *Greatcell solar materials*. All materials were used as received with no further purifications. Dipl was synthesized in our laboratories according to described procedures.

Pristine FASnI_3 precursor solution: 298 mg of SnI_2 (0.8 M), 137.57 mg of FAI (0.8 M) and 12.48 mg of SnF_2 (0.08 M) were dissolved in 1 mL of a binary mixture of DMSO:DMF (9:1, v/v) and stirred overnight at room temperature.

FASnI_3 precursor solution with NaBH_4 : 298 mg of SnI_2 (0.8 M), 137.57 mg of FAI (0.8 M), 12.48 mg of SnF_2 (0.08 M) and 1.9 mg of NaBH_4 (0.05 M) were dissolved in 1 mL of a binary mixture of DMSO:DMF (9:1, v/v) and stirred overnight at room temperature.

FASnI_3 precursor solution with Dipl: 298 mg of SnI_2 (0.8 M), 123.81 mg of FAI (0.72 M), 36.65 mg of Dipl (0.16 M) and 12.48 mg of SnF_2 (0.08 M) were dissolved in 1 mL of a binary mixture of DMSO:DMF (9:1, v/v) and stirred overnight at room temperature.

FASnI_3 precursor solution with Dipl and NaBH_4 : 298 mg of SnI_2 (0.8 M), 123.81 mg of FAI (0.72 M), 36.65 mg of Dipl (0.16 M), 12.48 mg of SnF_2 (0.08 M) and 1.9 mg of NaBH_4 (0.05 M) were dissolved in 1 mL of a binary mixture of DMSO:DMF (9:1, v/v) and stirred overnight at room temperature.

2.1.2 Assembly of SP-LFP devices

ITO coated glass was chemically etched with zinc powder and HCl (6 M) to obtain the desired ITO pattern, followed by a sequential washing process with soap-water, ethanol, acetone and isopropanol, respectively, in an ultrasonic bath for 15 minutes each. Then, the substrates were dried



with N₂ flow and subsequently introduced in an UV-Ozone lamp for 20 min. The PEDOT:PSS solution was filtered with 0.45 µm PVDF filter and spin coated on top of ITO at 5000 rpm (2000 rpm·s⁻¹ of acceleration) for 40s and annealed at 130 °C for 20 minutes in ambient conditions. After the HTL deposition the substrates were introduced in a N₂ filled glovebox, for the FASnI₃ layer deposition. The perovskite layer was deposited by one-step method with an antisolvent-based method, by adding FASnI₃ precursor solution (with or without additives) on top of PEDOT:PSS and spin coated at 4000 rpm for 50s. Then 400 µl of Chlorobenzene were dropped on top of the substrate after 20s of spinning, followed by a two-step annealing at 70 °C for 1 minutes and at 100 °C for 19 min. A 30 nm layer of C₆₀ was thermally evaporated on top of the perovskite layer as ETL, followed by 6 nm of BCP as buffer layer and 100 nm of Ag as metal contact. Then a light treatment was performed for 3 days under continuous illumination as part of device's fabrication procedure.

2.1.3 Characterization of SP-LFP films and devices

SEM images were taken with a field emission scanning electron microscope (FEG-SEM) JEOL 3100F) operated at 15 kV.

XRD pattern of the films were measured using X-ray diffractometer (D8 Advance, Bruker-AXS) (Cu K α , wavelength $\lambda=1.5406$ Å) with a Bragg angle range of 4-70° and step size of 0.05°.

Absorption spectra were registered on a Varian 20Cary300BIO UV/VIS spectrophotometer.

I-V curves and MPP in atmosphere conditions, were measured using an Abet technologies (Sun 2000) solar simulator. The light intensity was adjusted to 1 sun (100 mW·cm⁻²) using a calibrated Si solar cell and a photodiode. The devices were measured in ambient conditions without encapsulation, with an active area of 0.121 cm², defined by a shadow mask.

MPP and long-term stability measurements in N₂ conditions were measured under continuous illumination, using a Xenon lamp, by adjusting the sample-light source distance to set an optical power density of 100 mW·cm⁻², calibrated with a photodiode. The measurements were performed with an AUTOLAB (PGSTAT30) potentiostat; for the long-term stability measurements, an automatic sequence was set to measure the I-V curves every 2 hours. For the MPP measurements, a fixed voltage corresponding to VMPP was applied, which was obtained from the I-V curves, and the electrical current IMPP was monitored over time.

External quantum efficiency (EQE) measurements were performed with a QEPVSI-b Oriel system.

The steady-state PL measurements were registered using an intensified CCD (iStar 320 ICCD/DH320T-25U-03) coupled to a spectrograph (KYMERA-328I-B1) from Andor. A continuous diode-pumped solid-state laser module (532 nm, 150 mW max.) with controllable output power, model GL532RM-150 from SLOC LASERS, was used as an excitation source.

Time-resolved PL (TRPL) of thin films were measured at room temperature in vacuum conditions under excitation by 200 fs pulses from Ti:sapphire laser (Coherent Mira 900D) at a repetition rate of 76 MHz doubled to 405 nm with a BBO crystal. The backscattered PL signal was dispersed by a double 0.3-m focal length grating spectrograph/spectrometer (1200 g/mm with 750 nm blaze) and detected by a Si micro photon device (MPD) and single-photon avalanche diode (SPAD) photodetector (connected through a multimode optical fiber to the monochromator); the SPAD was attached to a time correlated single photon counting electronic board (TCC900 from Edinburgh Instruments). The excitation fluence is 15 nJ.cm⁻², the instrument response function (IRF) is about 50 ps.



2.2 Fabrication of tin-based B-LFPs solar cells

The focus of the experimental work was the production of optoelectronic devices with the architecture shown in figure 8.

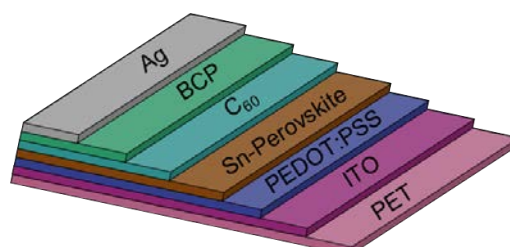


Figure 8. Architecture of the benchmark Sn-based LFP.

2.2.1 Ink preparation

Reagents were purchased from commercial vendors and used as received unless mentioned otherwise. For blade coating the typical ink preparation SnI_2 (99.999% Mesh Beads, Sigma-Aldrich), SnF_2 (99%, Acros Organics) and FAI (Dyanamo) were mixed in a molar ratio of 1:0.1:1 for a concentration of 0.76 mol L^{-1} . The precursors were dissolved in either anhydrous DMF (Sigma-Aldrich)-DMSO (≥ 99.9 , Sigma-Aldrich) 4:1 volume ratio, or acetonitrile (99.8%, Sigma-Aldrich)-gamma-butyrolactone (Sigma Aldrich) 9:1 volume ratio and stirred at room temperature until a clear yellow solution was obtained; before use they were passed through a $0.22 \mu\text{m}$ filter. Methylammonium acetate (MAAc) was synthesized from acetic acid (99.8%, Sigma-Aldrich) and methylamine (33% solution in ethanol, Sigma-Aldrich), a solid was purified via rotary evaporation and stored inside a glovebox to avoid moisture absorption; this additive was incorporated into the inks in a molar ratio between 0.5-2.

In the case of inkjet printing the precursors were dissolved in different anhydrous solvent systems (Sigma-Aldrich): DMF-DMSO (4:1 or 9:1 volume ratio), GBL:DMSO (7:3 volume ratio), ACN-2ME (3:2 volume ratio). The inks were filtered using a PTFE filter with a $0.22 \mu\text{m}$ pore size and injected into compatible Fujifilm cartridges, that were previously left under vacuum for 30 min to remove residual moisture.

2.2.2 Device assembly

All HTM layers were prepared with an Erichsen Coatmaster 510 blade coater; first the PET-ITO substrates were cut to a suitable size and the pattern was etched with a laser marking system from Rofin (PowerLine E Air 25); then they were cleaned and treated with a plasma cleaning system (PE-75 Plasma Etch) before being covered with a PEDOT:PSS aqueous dispersion (Clevios P VP Al 4083, Heraeus), previously sonicated and passed through a $0.45 \mu\text{m}$ filter. The substrates were annealed in an oven at $100 \text{ }^\circ\text{C}$ for 40 minutes to remove any residual moisture from the surface before transferring to a glovebox for the perovskite processing.

The perovskite film was deposited either by blade coating or inkjet printing; after drying the substrates were annealed on a hotplate for 20 minutes at a standard temperature of 85°C . The remaining layers of C_{60} (98%, Sigma Aldrich), BCP (99.99%, Sigma Aldrich) and Ag (pellets, Kurt J Lesker) were thermally evaporated (Glovebox Integrated MB ProVap connected to an Inficon SQC-310C Thin Film Deposition Controller) to complete the devices.

In the case of inkjet printing, several operational parameters were tested to optimize the quality of the perovskite layer; the drop spacing was varied between 20-200 μm , and the platen was heated to temperatures between 30-60 $^\circ\text{C}$; furthermore, the effect of a pre-annealing treatment under



vacuum or a diethyl ether bath were also evaluated. Additionally, the impact of additives/surfactants was investigated: BAAC 0-20 $\mu\text{L}/100 \mu\text{L}$ solution was introduced to help control the crystallization/drying process, butyl acetate (BuAc) 5-10% V/V and α -phosphatidylcholine (α -PC) 0.2-0.8 mg/mL were included in the formulation with the aim to improve the wettability of the ink. The morphological condition of these films was recorded using a Tamkly wireless digital microscope, and evaluated by means of XRD-SEM; the thickness measurements were performed with a Dektak XT stylus profilometer.

To inspect the architecture and layer properties of the completed devices a cross section was analysed with a SEM/Xe-PFIB microscope.

2.2.3 IV Characterization

The IV curve of the devices was measured with a solar simulator (Sun 2000 ABET Technologies) equipped with a Keithley 2450 SourceMeter, previously standardised to 1 Sun (1000 W m^{-2} irradiance, AM 1.5G) with a Si reference cell (15150 ABET Technologies T). The solar cells were also tested at in a low light set up, calibrated for 1000 lux with a Light Meter (HD450 Exttech).

2.2.4 Passivation strategies for improved stability

As an attempt to enhance the stability of the devices a passivation layer was deposited on top of the perovskite film, with the hopes of smoothing the surface from defects and pin holes, as well as to promote encapsulation from atmospheric oxygen and moisture. The essays were performed with n-octylammonium iodide (OAI, Greatcell), phenethylammonium iodide (PEAI, Greatcell), butylammonium acetate (BAAC) and tetrabutylammonium iodide (TBAI, >99% Sigma-Aldrich); the solutions (3 mg/mL n-butanol) were blade coated immediately after the thermal annealing of the main absorber layer and before the evaporation of the ETM.

2.2.5 Tests with alternative ETMs

C₆₀ (>99.5, TCI), PCBM (>99.5, Lumtec) and ICBA (>99%, Ossila) were dissolved in chlorobenzene (20 mg/mL) and deposited through blade coating. These experiments were executed with the goal of optimizing band alignment for the perovskite/ETM interface and to explore the possibility of devices with fully solution-processed charge transport and absorber layers, which could be valuable for industrial-scale fabrication.

3 Results

3.1 SP-LFP films and devices

3.1.1 Morphological and structural characterization of SP-LFP

Aimed at improving the performance and stability of FASnI₃ based solar cells, a series of additives were incorporated into the LFP precursor solutions. On one hand the reducing agent NaBH₄ was considered for preventing the problematic Sn⁺² oxidative degradation. On the other hand, Dipl, a bulky alkylammonium cation was introduced for passivation purposes; additionally, the combination of both additives was also investigated pursuing their potential synergistic impact on the device's performance. Figure 9 shows the morphological and structural characterization of the pristine FASnI₃ and those samples containing Dipl, NaBH₄ and their combination, respectively. Figure 9a corresponds to the SEM image obtained for the pristine FASnI₃ film, which shows an inhomogeneous grain distribution, with presence of numerous pinholes and significant grain size polydispersity. This phenomenon has been extensively reported due to the fast crystallization and solvent-induced Sn⁺²

oxidation during the preparation of LFP precursors solution and film deposition. Interestingly, a clear beneficial effect on the morphological features of FASnI_3 films is observed upon the incorporation of our additives.

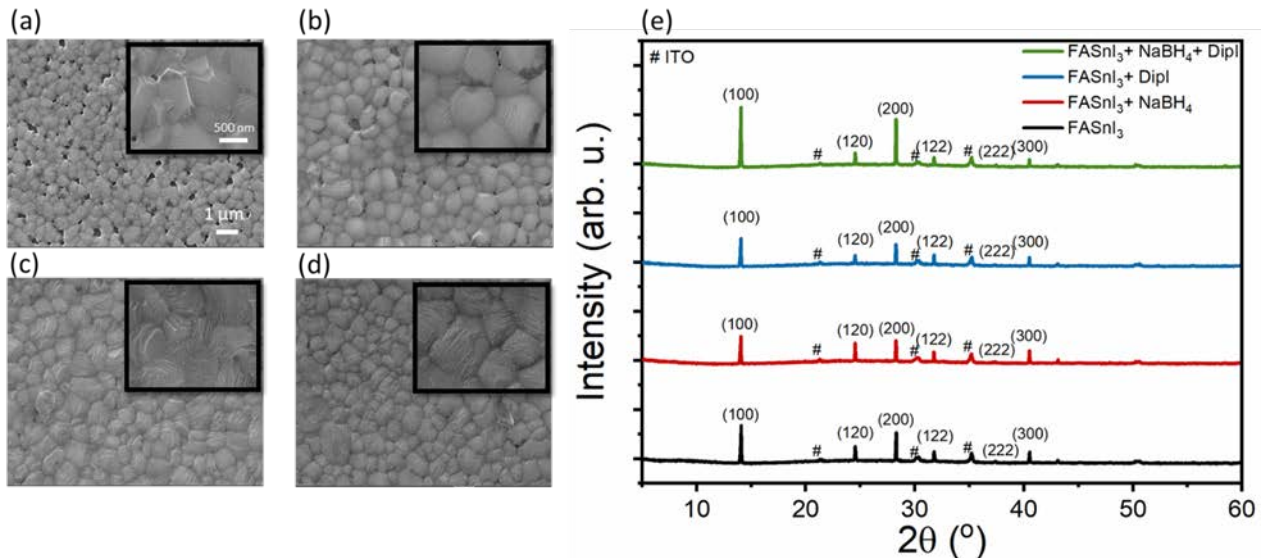


Figure 9. Morphological and structural characterization of **Sn-HPS** films. (a-d) Top view SEM images of (a) FASnI_3 , (b) FASnI_3 +Dipl, (c) FASnI_3 + NaBH_4 , and (d) FASnI_3 +Dipl+ NaBH_4 films. (e) XRD pattern of FASnI_3 films with different additives; # indicate the diffraction peaks of ITO. SEM images a-d were registered at the same magnification and therefore, the scale-bars are equivalent.

Particularly, the addition of Dipl induces the formation of slightly larger crystals with more defined shapes and lower surface roughness compared to the pristine films; yet, the presence of pinholes is still detected (Figure 9b). Contrarily, when NaBH_4 is incorporated into the FASnI_3 precursor solution (Figure 9c), a very compact and pinhole-free layer is obtained. Strikingly, those films obtained in the presence of both additives (Figure 9d), revealed the beneficial effects provided by both chemical species; *i.e.* excellent surface coverage without the presence of pinholes, large and well-defined crystalline domains and lower surface roughness. The crystalline structure is very similar in all FASnI_3 films without and with additives.

3.1.2 Optical characterization of the SP-LFP films

The optical properties of the FASnI_3 films obtained through spin-coating of the corresponding precursor solutions with additives were studied and the results compared with those from the pristine LFP films. As it is shown in Figure 10a, the absorption spectra of FASnI_3 with and without additives are very similar, although a slight decrease in the absorbance is systematically observed upon the addition of Dipl. Besides, the addition of Dipl slightly blue-shifts the band edge absorption position, as it is shown in the inset of Figure 10a; this small hypsochromic shift together with the decrease in the absorbance along the UV-VIS-NIR spectral range has been previously observed and it was ascribed to the insertion of the bulky cation into the perovskite structure.

The photoluminescence (PL) spectra of both FASnI_3 and $\text{FASnI}_3 + \text{NaBH}_4 + \text{Dipl}$ samples were practically identical (roughly, $\lambda_{\text{max}} = 880$ nm and FWHM = 57 nm), although, accordingly to the absorption spectra, an almost unperceivable blue-shift of 4 nm is observed for the sample containing both additives, see Figure 10b. These results indicate that the use of Dipl and NaBH_4 do not induce dramatic changes in the absorptive and emissive properties of the HPS bulk, even though the bulky

cation is inserted into the HPS structure. However, time-resolved PL spectroscopy (TRPL) clearly revealed that the addition of Dipl and NaBH_4 increases the charge-carrier lifetime beyond a 107% compared to pristine FASnI_3 (Figure 10c), $\tau = 1.37$ vs 0.61 ns, respectively, thus meaning that the additives lead to an efficient inhibition of the non-radiative recombination pathways.

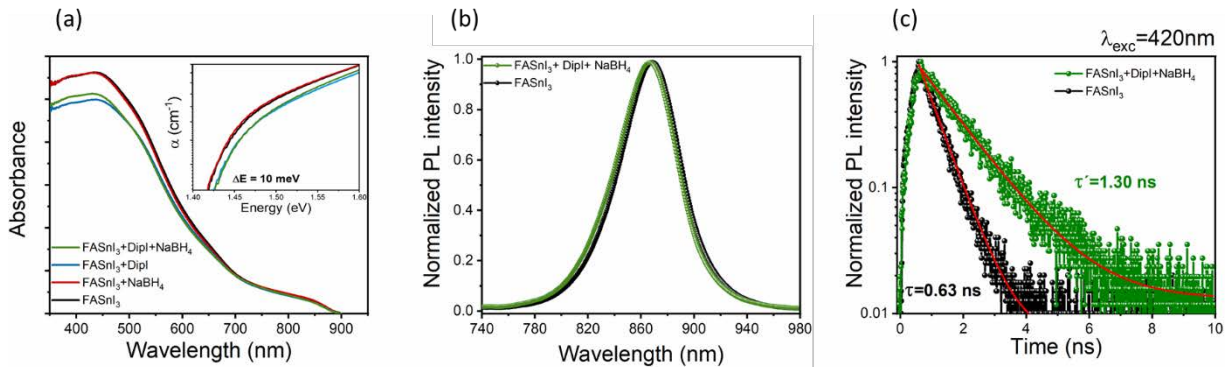


Figure 10. Optical characterization of SP-LFP films deposited on glass: (a) UV–Vis spectra of FASnI_3 films without and with different additive formulations; inset shows the absorption coefficient, α , as function of energy in the absorption band edge region, (b) Normalized PL spectra and (c) Time-resolved PL decays corresponding to FASnI_3 without and with both additives. The first parts of the PL decays were fitted to monoexponential functions.

3.1.3 Characterization of the SP-LFP devices under 1-sun illumination

Once fabricated, the resulting SP-LFP devices were characterized under the solar simulator for the assessment of their performances. Figure 11 shows the performance of the devices obtained from the different additive formulations.

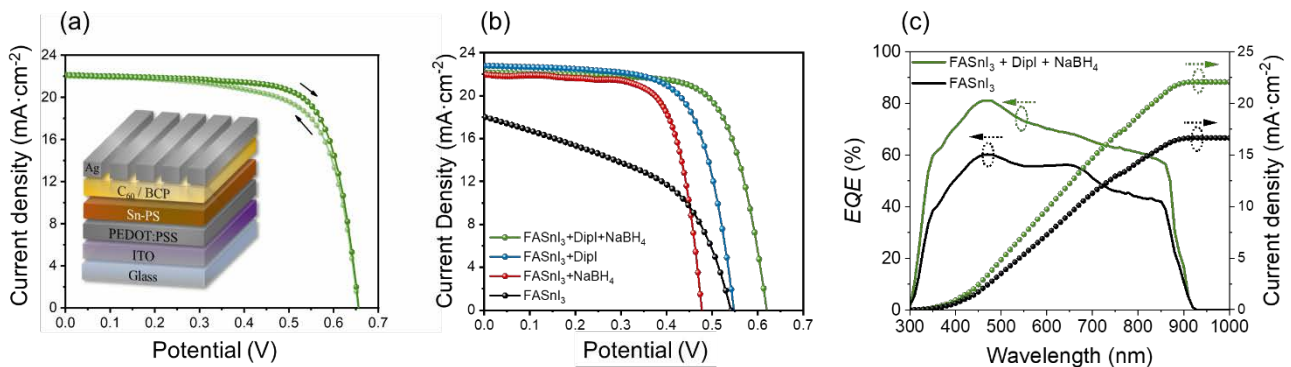


Figure 11. Photovoltaic performance. (a) forward (F-) and reverse (R-) scans of the I-V curve for the champion $\text{FASnI}_3+\text{Dipl}+\text{NaBH}_4$ device; the inset shows the schematic configuration of the device. (b) F-scan of I-V curves for FASnI_3 devices (without and with different additives) that are representative of the average behaviour. (c) External quantum efficiency and integrated current obtained from the FASnI_3 and $\text{FASnI}_3+\text{Dipl}+\text{NaBH}_4$ devices. The I-V curves and EQE spectra were measured after 3 days of light-soaking treatment.

For reliability reasons, an exhaustive statistical study of the device's performances was carried out (Figure 12), which consisted on averaging the cell parameters obtained from fresh and aged devices upon 3-days under continuous illumination in inert atmosphere, all of them prepared in the same batch.

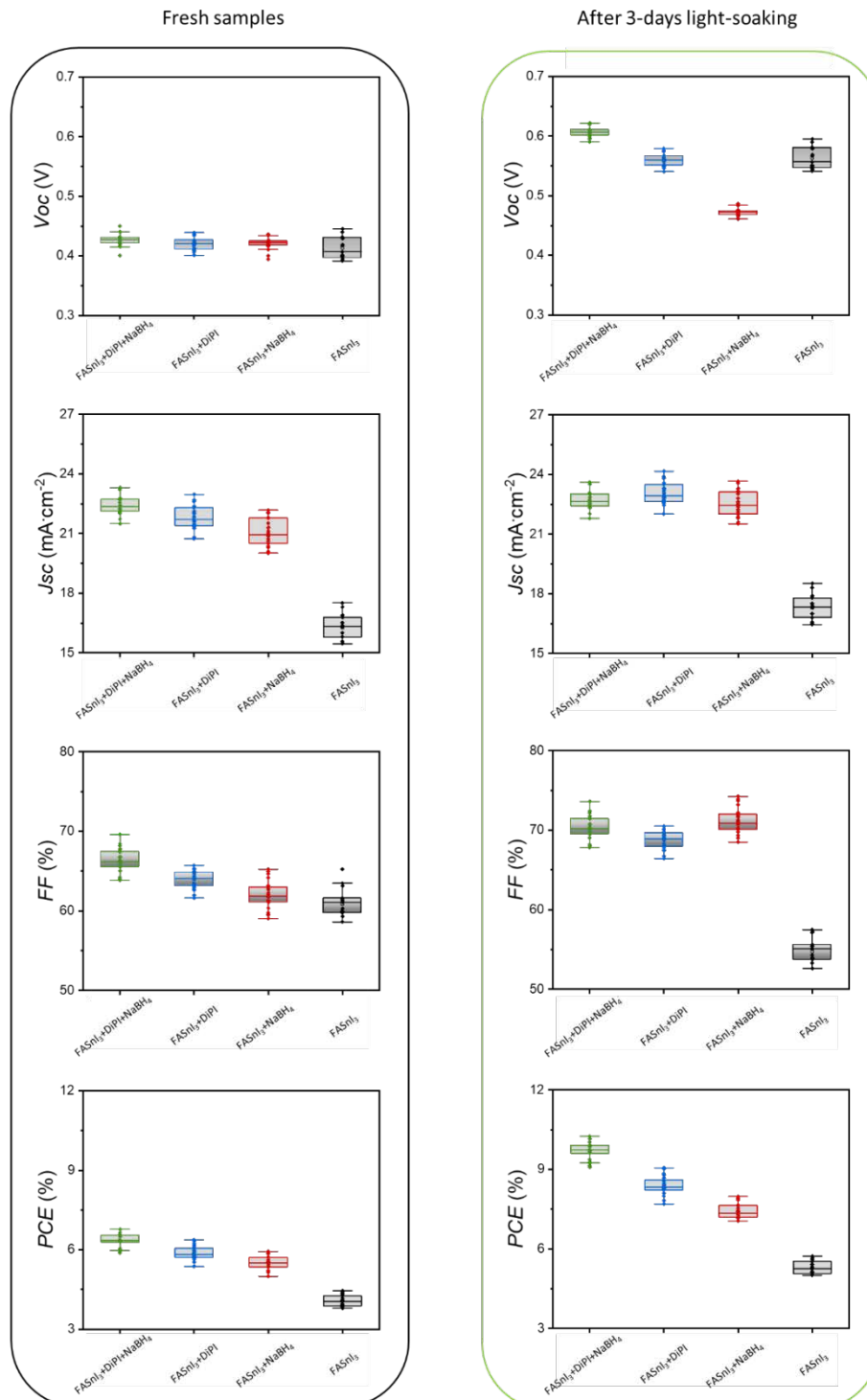


Figure 12. Averaged cell parameters of the fresh and aged devices upon 3-days under continuous illumination in inert atmosphere; all these cells were prepared in a single batch for a fairer comparison.

The long-term stabilities of the SP-LFP devices were also investigated. Figure 13a shows the efficiency and current density of the FASnI₃+DIPi+NaBH₄ obtained from monitoring the device at maximum-power-point (MPP) in ambient conditions (air at ~60% RH) without encapsulation. These



results evidence that the devices with both additives show enhanced stability even in harsh conditions. Figure 13b shows the evolution of the normalized efficiency of the pristine FASnI_3 and $\text{FASnI}_3+\text{Dipl}+\text{NaBH}_4$ devices, respectively, extracted from I-V curves measured at different times of constant illumination in inert atmosphere. Even though both devices show a similar initial PCE increase during the first ~ 40 hours, the sample without additives experienced a steep premature degradation that was not observed for the samples containing both additives; in fact, the efficiency of the $\text{FASnI}_3+\text{Dipl}+\text{NaBH}_4$ increased gradually during the first 400 hours at constant illumination. Figure 13c displays the normalized efficiency extracted from the monitoring at MPP in inert atmosphere obtained from the reference FASnI_3 device and $\text{FASnI}_3+\text{Dipl}+\text{NaBH}_4$, respectively.

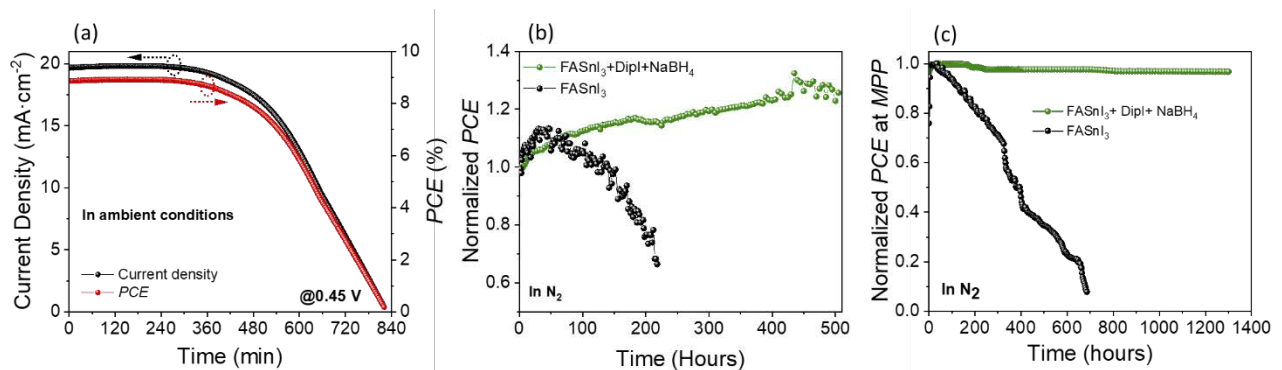


Figure 13. Stability of Devices. (a) Stability test under illumination (AM1.5G , $100 \text{ mW}\cdot\text{cm}^{-2}$) of the $\text{FASnI}_3+\text{Dipl}+\text{NaBH}_4$ device at MPP in ambient conditions ($\sim 60\%$ RH) without encapsulation. (b-c) Stability comparison of the unencapsulated FASnI_3 and $\text{FASnI}_3+\text{Dipl}+\text{NaBH}_4$ devices under continuous illumination (1 sun) every 2 hours in N_2 atmosphere and (c) normalized PCE at MPP in N_2 atmosphere.

All these results clearly demonstrate the beneficial contribution of Dipl and NaBH_4 additives towards the development of highly efficient and durable Sn-based solar cells, whose performance will be considered as a benchmark for subsequent fabrication of devices based on blading and inkjet printing procedures.

3.2 Blade coated tin-based perovskite solar cells under 1 sun illumination

The finished solar cells (figure 14) appearance was dependent on the processing speed/thickness of the perovskite, but most devices had dark homogenous perovskite layers and reflective contacts without noticeable defects.

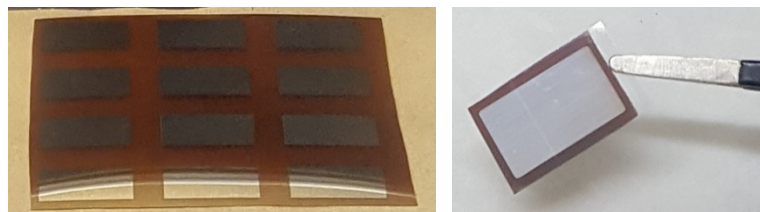


Figure 14. Completed devices in matrix and single cell.

As reported in deliverable 3.1, when blade coating was used to deposit the perovskite film, the morphology and quality was highly dependent on factors like the ink formulation and the blade coating speed. Thus, the photovoltaic properties were compared between batches in the range of $0.7\text{-}5 \text{ mm s}^{-1}$ (figure 15); for both inks systems ($\text{ACN}:\text{GBL}$ and $\text{DMF}:\text{DMSO}$) there was a trend with maximum points around $1\text{-}2 \text{ mm s}^{-1}$, with lower efficiencies at higher velocities.

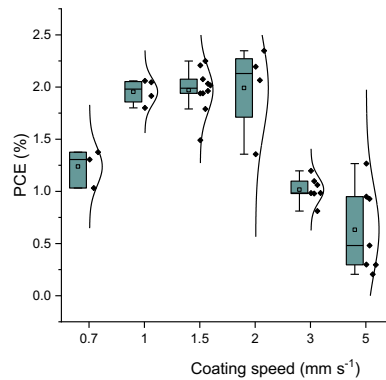


Figure 15. Variation of device efficiency vs coating speed for ACN:GBL solvent system.

When these results were analyzed coupled with the cross-section images of the devices (figure 16), it seems like the thicker layers obtained at higher speeds (figure 17) generated troubles for the operation of the solar cells.

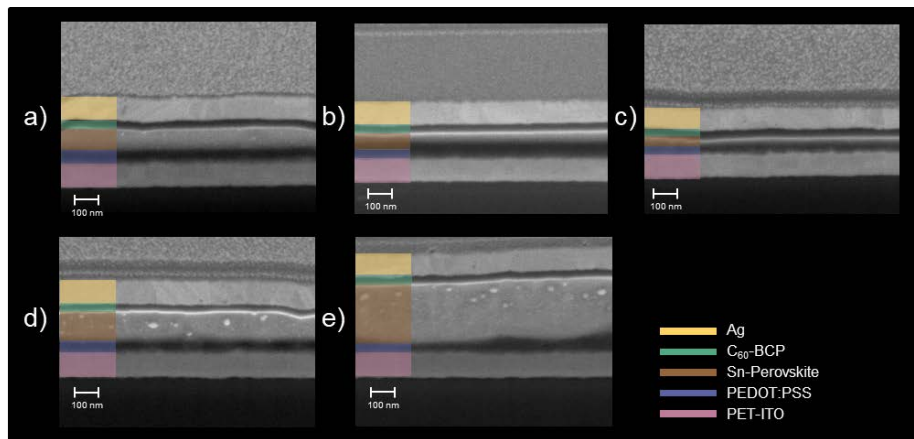


Figure 16. Cross section images of devices blade coated from ACN:GBL inks at different speeds: a) 0.7 mm s⁻¹ b) 2 mm s⁻¹ c) 3 mm s⁻¹ d) 5 mm s⁻¹ e) 10 mm s⁻¹.

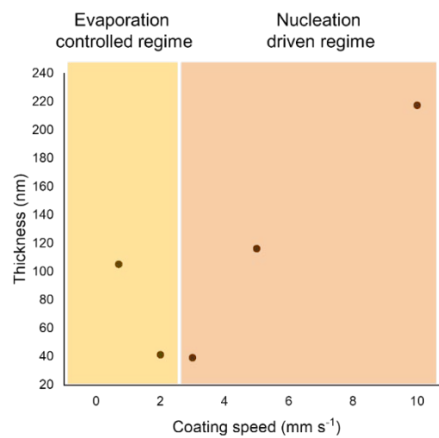


Figure 17. Perovskite film thickness relation to blade coating speed for ACN:GBL inks.

The I-V properties of the best performing devices are summarized in figures 18-19 and table 1. Both the V_{OC} and J_{sc} were lower than expected, and slight hysteresis was detected in some cases; it is



evident that there is room for improvement and more work should be made focused on minimizing defects at the interface between the perovskite and the charge transport materials.

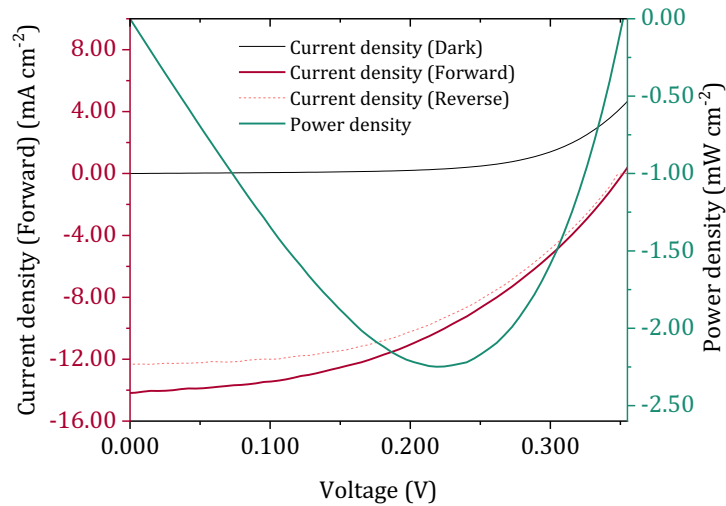


Figure 18. I-V curve of cell fabricated with a coating speed of 1.5 mm s⁻¹.

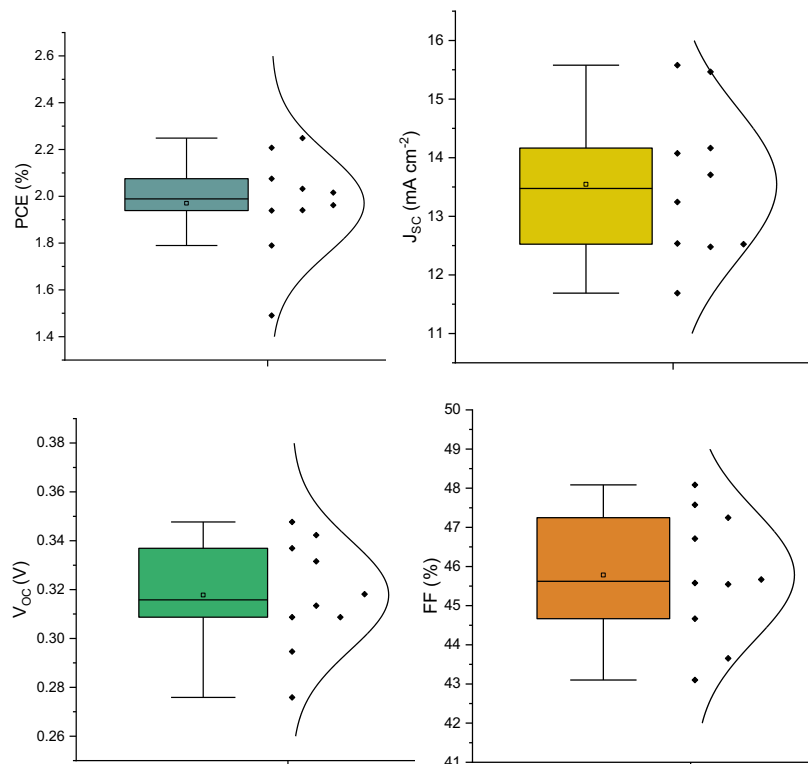


Figure 19. Photovoltaic properties of devices fabricated with a coating speed of 1.5 mm s⁻¹ under 1 sun illumination.



Table 1. Average and best I-V parameters of cells under 1 Sun conditions.

	J_{SC} (mA·cm ⁻²)	V_{oc} (V)	FF (%)	PCE (%)
Average	13.5 ± 1.3	0.32 ± 0.02	45.8 ± 1.7	2.0 ± 0.2
Best	15.6	0.31	45.6	2.2

3.3 Blade coated tin-based perovskite solar cells under low light conditions

In general, when the devices were tested under low light conditions (1000 lux, irradiance 3.14 mW cm⁻²) the I-V curve behavior and photovoltaic properties (figures 20-21) were similar, with a small improvement in the fill factor (table 2).

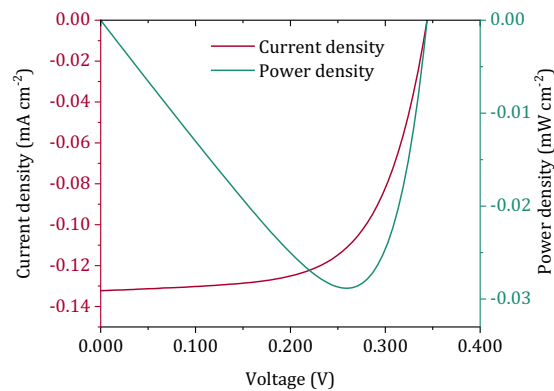


Figure 20. I-V Curve of best performance cell under low light conditions.

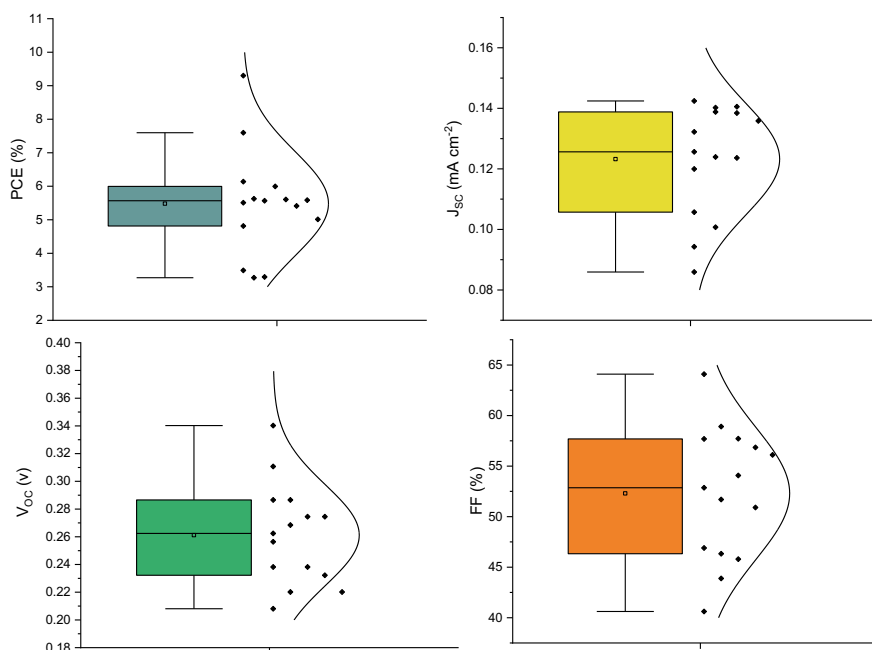


Figure 21. Photovoltaic properties of devices fabricated with a coating speed of 1.5 mm s⁻¹ under 1000 lux illumination.



Table 2. Average and best I-V parameters of cells under low light conditions.

	J_{SC} (mA·cm ⁻²)	V_{oc} (V)	FF (%)	PCE (%)
Average	0.123 ± 0.018	0.26 ± 0.04	52.3 ± 6.5	5.5 ± 1.6
Best	0.132	0.34	64.1	9.3

3.4 Passivation strategies for improved stability

When cells were taken outside the glovebox to be measured, a rapid decay in efficiency was noticed over time (figure 22). With the introduction of bulky organic cations (tetrabutyl ammonium TBA, butylammonium BA, phenethylammonium PEA, octylammonium OA) as a coating, the layers turned visually darker and smoother, but when the reference cells without a passivation layer were measured the results were consistently better. The main issue could be traced to a dramatic decrease in current, and since no considerable improvement in the stability of the devices was noticed, it was concluded that passivation strategies brought no advantages under the tested conditions.

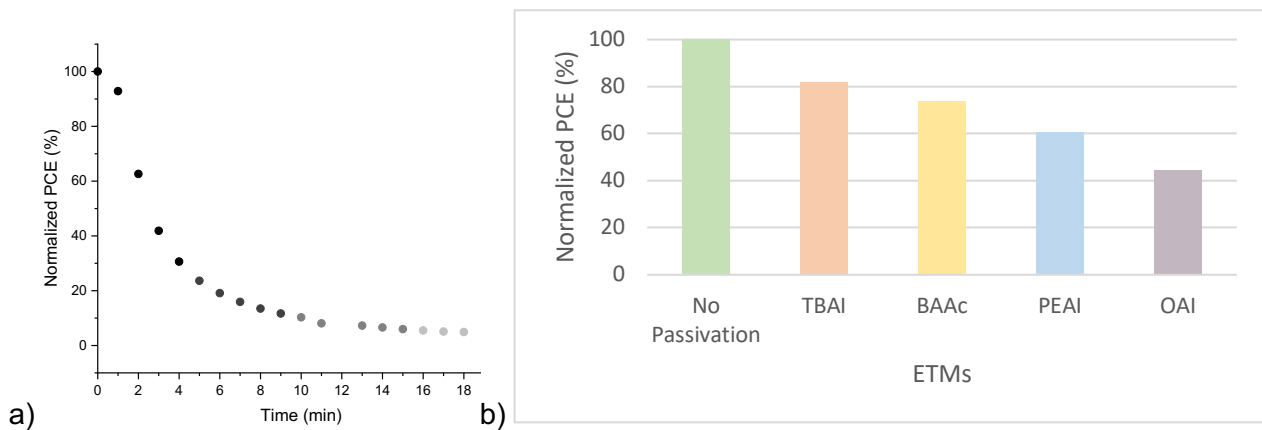


Figure 22. a) Decay of efficiency over time. b) Relative efficiency of devices with and without passivation.

3.5 Tests with alternative ETMs

Comparing the blade coated ETMs to the reference cells fabricated with thermally evaporated C₆₀ showed a decrease in the photovoltaic properties (figure 23), even if ICBA seemed to have potential to improve the V_{oc} it was outbalanced by lower currents and FF; both the blade coated C₆₀ and PCBM had worse performance overall. These results indicate that although it is possible to deposit the ETM with the blade coating technique, much work is needed to optimize the quality of the film and the interface with the perovskite layer.

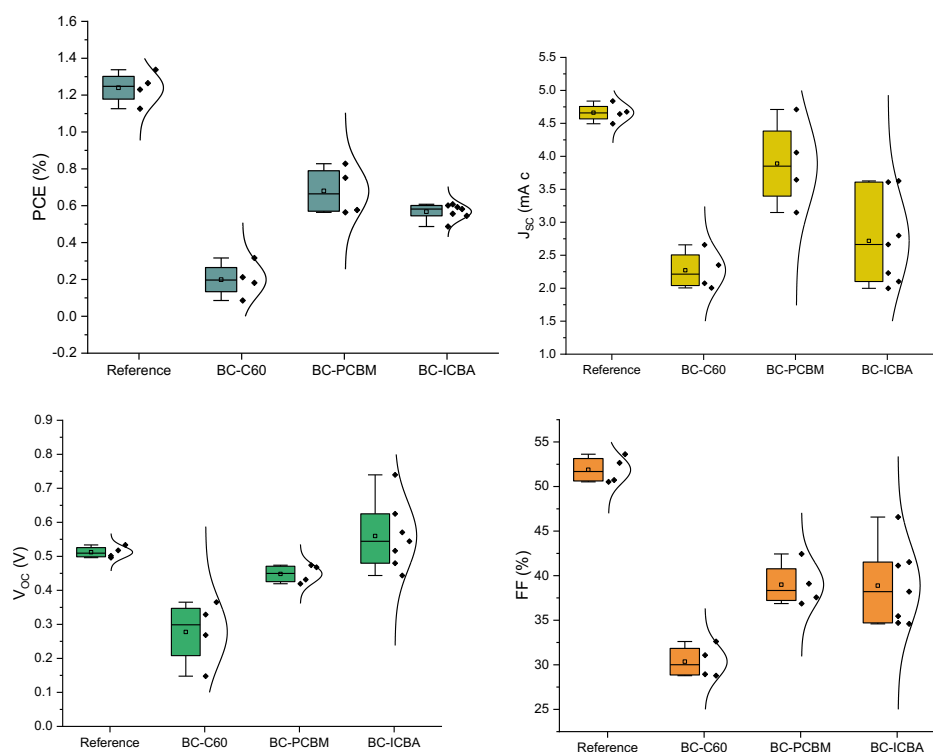


Figure 23 Photovoltaic properties of reference cells with evaporated C₆₀ and alternative blade coated (BC) ETMs.

3.6 Inkjet-printed tin-based perovskite

3.6.1 Print quality tests

The quality of the printed layers was evaluated based on several factors:

- **Print resolution:** the drops are placed close enough to coalesce but also far apart to ensure a complete surface wetting.
- **Print definition:** the edges of the print area are well defined, there is no discernible bleeding out or evidence of wet film shrinkage.
- **Uniformity:** the whole area has similar characteristics, without visible diffusion waving or printing patterns; there is no fading or other indication of thickness gradients.
- **Drying profile:** there is no evidence of coffee ring effect, and the evaporation-crystallization processes occur in a controlled manner before annealing.
- **General appearance:** the final film should be smooth, reflective, dark and opaque.

Table 3 shows the images of layers printed using the DMF:DMSO (4:1) ink system and W1 waveform, in all the samples two distinct regions were detected. The first one with a rougher appearance corresponds to the area where the deposition begins, while the second one is more homogeneous but thinner, and extends from the final printing zone; increasing the drop spacing seemed to generate a larger and more uniform first region, probably because there is a smaller amount of liquid to spread around and the process is shorter, leaving less chance for diffusion. Moreover, raising the substrate platen temperature (T) had a similar effect at 45 °C, but above this

temperature larger solid clusters form on the surface and the ink starts to bleed out from the edges; applying vacuum for a couple of minutes before annealing resulted in a completely different look, the samples were smoother and darker, but still not reflective nor homogeneous.

Table 3. Photographs of printed layers with waveform W1 and DMF:DMSO (4:1) ink.

V: 20 mV, T: 30 °C			
DS: 20 μm	DS: 25 μm	DS: 30 μm	DS: 45 μm
V: 20 mV			
DS: 30 μm T: 45 °C	DS: 30 μm T: 60 °C	DS: 20 μm T: 30 °C + Vacuum	DS: 30 μm T: 30 °C + Vacuum

In contrast to blade coating, without the N₂ quenching the printed layers did not show a clear change from wet yellow ink into the dark brown intermediate phase before annealing, which was a key feature for obtaining superior perovskite films; thus, the impact of pre-annealing treatments to trigger this transition was studied further (table 4). Some samples were dipped into diethyl ether (Et₂O) as an antisolvent bath, unfortunately upon contact the liquids intermixed and produced heterogenous layers with diverse textures and morphologies; when other samples were left under vacuum in the glovebox antechamber small cubic crystals connected by a mesh of crosshatching needles were observed, instead of the branched and irregular trapezoid structures when the substrates were directly placed on the hot plate.

Table 4. Pre-annealing treatment effect on the morphology of printed layers with waveform W1 and DMF:DMSO (4:1) ink.

Conditions	Images
<p>T: 30 °C No treatment</p>	<p>DS: 20 μm DS: 30 μm</p>
<p>T: 30 °C Et₂O bath (long)</p>	
<p>T: 30 °C Et₂O bath (short)</p>	

<p>T: 45 °C Vacuum</p>	
<p>T: 45 °C Et₂O bath (short)</p>	

The 9:1 ink produced slightly more uniform layers; the images displayed in table 5 have similar trends as the case described before, without any treatment isolated nucleation points are observed not matter the drop spacing used. Vacuum leads to either a mixture of small cubes and thin needle crystals with varying pinhole density or globular domains at higher DS; the Et₂O bath appeared to favour plate-like structures and proved that more uniform coverage can be obtained in the microscale, but still the process is not practical or reliable from a technical point of view.

Table 5. Pre-annealing treatment effect on the morphology of printed layers with waveform W1 and DMF:DMSO (9:1) ink, T: 30 °C.

Conditions	Images
<p>DS: 25 μm No treatment</p>	

<p>DS: 25 μm Vacuum</p>	
<p>DS: 25 μm Et₂O bath</p>	
<p>DS: 35 μm No treatment</p>	

<p>DS: 35 μm Vacuum</p>	
<p>DS: 35 μm Et₂O bath</p>	

<p>DS: 45 μm No treatment</p>	
<p>DS: 45 μm Vacuum</p>	
<p>DS: 45 μm Et₂O bath</p>	

The overall substrate coverage was also dependent on the drop spacing (figure 24), when a separation of more than 125 μm was applied the printed pattern could be seen even with the naked eye and the coalescence of the film was compromised at higher DS values.

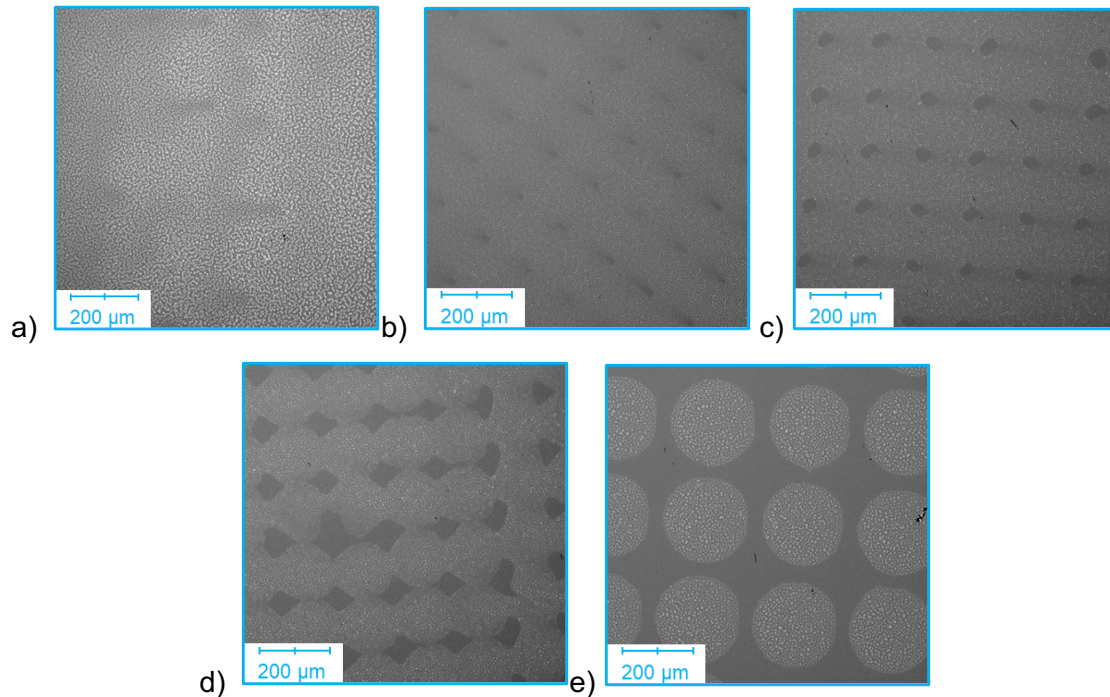
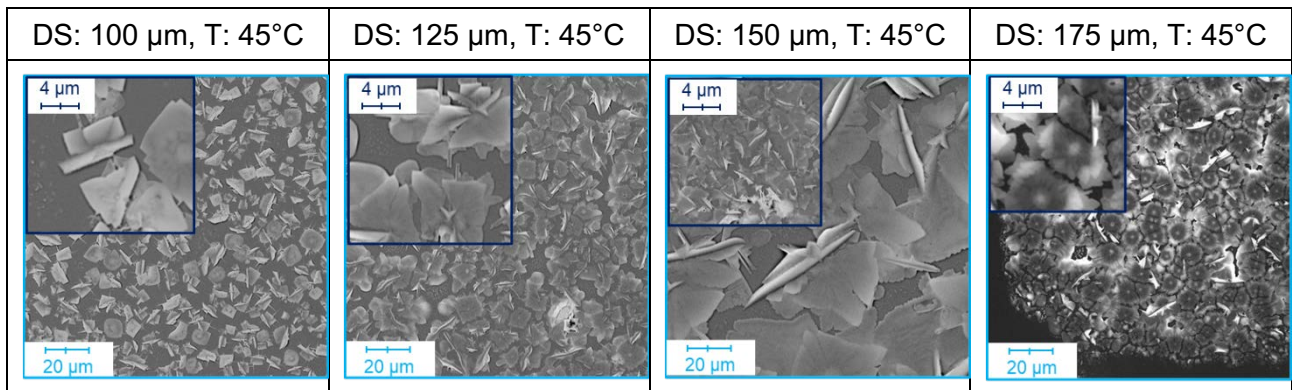


Figure 24. Inkjet-printed layers deposited with a drop spacing of
 a) 125 μm b) 150 μm c) 155 μm d) 160 μm e) 165 μm .

However, when looking closer (table 6), at lower drop spacing less area was coated in perovskite, and when the droplets were more disconnected the crystals grew closer together; even though the films seemed more homogeneous, the SEM images showed drastically different morphologies between the samples, thus DS is a key parameter to consider during the deposition. At the same time, increasing the platen temperature had a negative effect on the crystallinity and coverage of the perovskite.

Table 6. Effect of drop spacing and deposition temperature on inkjet-printed perovskite morphology.

Ink concentration 0.4 mol L ⁻¹ , WF: LV, nozzle jetting voltage 25 V, BAAC: 3 $\mu\text{L}/100 \mu\text{L}$ solution.			
DS: 100 μm , T: 30°C	DS: 125 μm , T: 30°C	DS: 150 μm , T: 30°C	DS: 175 μm , T: 30°C



Besides the DS and heating conditions the most influential effect was seen with the implementation of butylammonium acetate as an additive (figure 25). Without the ionic liquid almost no crystal formation was observed, and the layers were rough and grey; upon the incorporation of BAAC the layers formed an intermediate phase during the deposition and resulted in darker reddish films. The best outcomes were recorded for a concentration of 10 μL BAAC/100 μL of solution, at higher quantities a coffee ring effect was enhanced.

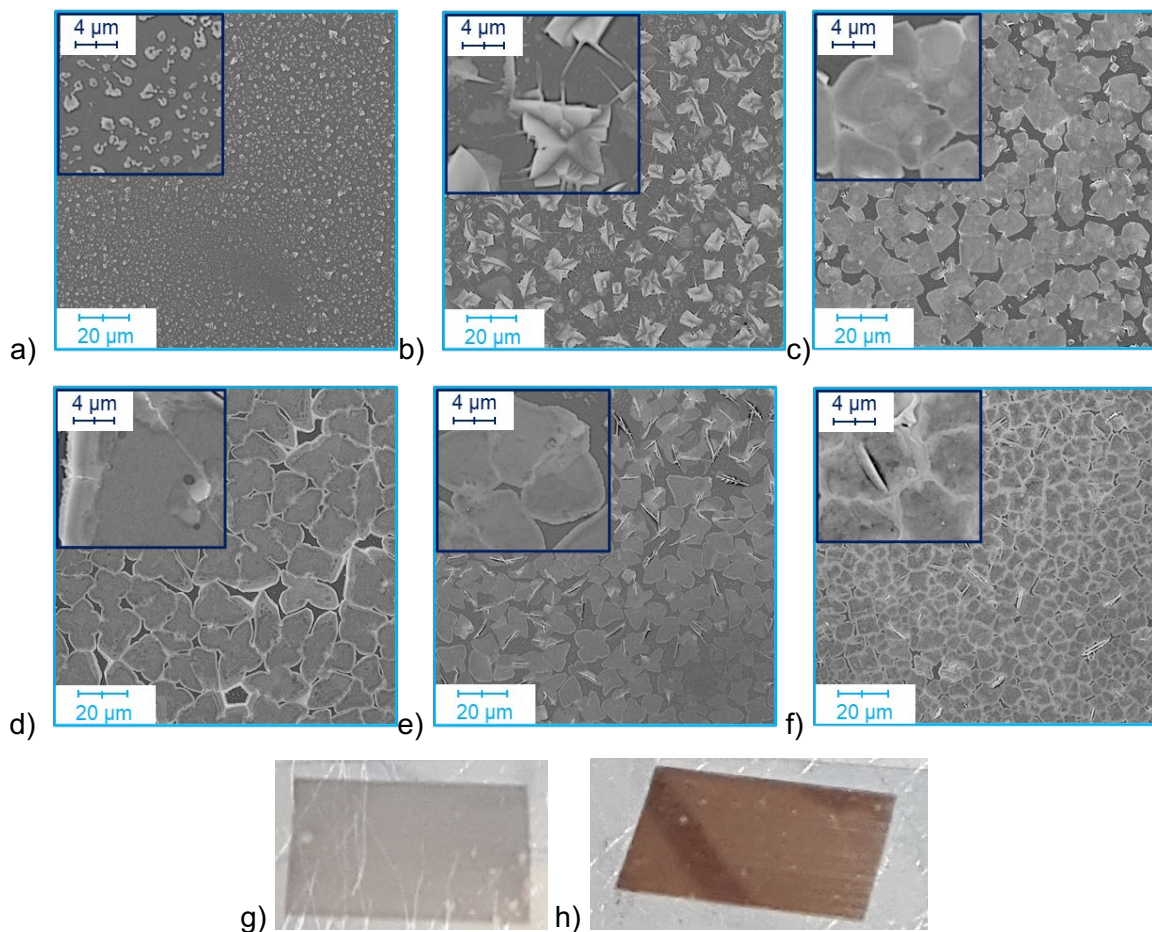


Figure 25. Inkjet printed layers, WF: LV, DS 100 μm , with varying BAAC (per 100 μL of solution)

a) 0 μL b) 2.5 μL c) 5 μL d) 10 μL e) 15 μL f) 20 μL g) layer without BAAC h) layer with BAAC.

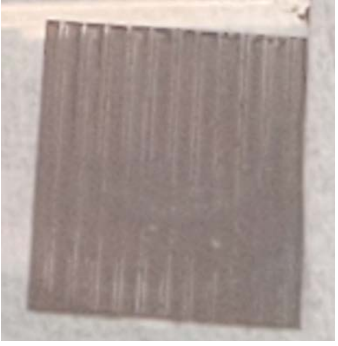



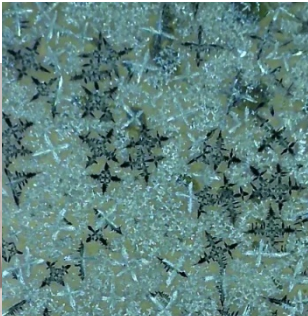

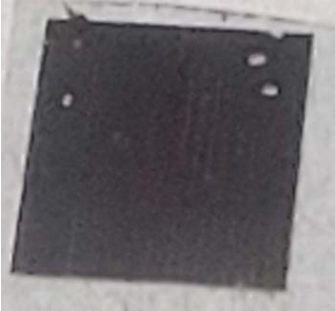





Following these outcomes, other additives were introduced into the precursor to see if the morphology could be better controlled at lower DS (table 7). The ink with butyl acetate (BuAc) had a slight improvement in comparison to the standard, but the change was not on the same level as with the ionic liquid; when used in combination with the BAAC the formation of larger crystal domains was retained with the best results at a DS of 75 μm . The surfactant (α -PC) mainly helped with the wettability, nonetheless it also changed the morphology to a wirelike framework with a lot of voids.

Table 7. Effect of additive mixtures on inkjet-printed perovskite morphology.




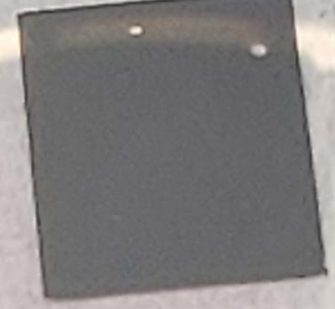
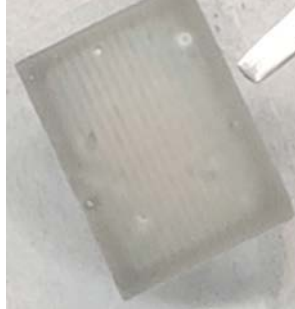




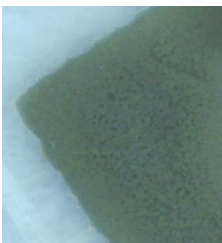




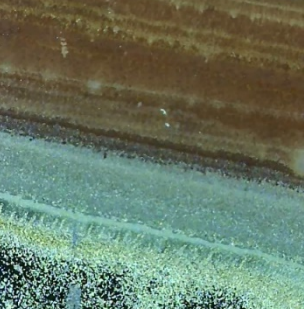

Ink concentration 0.4 mol L^{-1} , WF: LV, DS: $75 \mu\text{m}$, nozzle jetting voltage 20 V, T: 30°C			
+ 5% BuAc	+ 10% BuAc	+ 0.8 mg/mL α -PC	
+ 10% BuAc + 10 μL BAAC/100 μL solution			
DS: $45 \mu\text{m}$	DS: $75 \mu\text{m}$	DS: $100 \mu\text{m}$	DS: $125 \mu\text{m}$

Using these conditions, a deposition with a large area for devices ($80 \times 80 \text{ mm}^2$) was performed (table 8), and some issues were noticed, both the coverage and perovskite crystal formation were different when compared to the smaller scale test. Lower DS and a series of increasing voltages were tested to try to improve the print resolution, to compensate for the thicker wet layer a vacuum assisted drying step was performed before the annealing. Although the coverage improved after 30 mV, the coffee ring effect was also more pronounced; this was somewhat resolved with the addition of BuAc, but then again when the size of the print was extended the crystallization process had an unpredictable behaviour leaving a heterogenous layer.

Table 8. IP results of precursor with 10 μL BAAC/100 μL solution, ink concentration: 0.4 mol L⁻¹, WF: LV, T: 30 °C.

Conditions	Images		
DS: 75 μm V: 40 mV Print area: 20x16 mm ²			
DS: 75 μm V: 40 mV Print area: 80x80 mm ²			
DS: 45 μm V: 20 mV Vacuum			
DS: 45 μm V: 25 mV Vacuum			



<p>DS: 45 μm V: 30 mV Vacuum</p>				
<p>DS: 45 μm V: 35 mV Vacuum</p>				
<p>DS: 45 μm V: 40 mV Vacuum</p>				
<p>+ BuAc DS: 45 μm V: 40 mV Vacuum</p>				
<p>+ BuAc DS: 45 μm V: 40 mV Print area: 80x80 mm²</p>				

Based on encouraging results obtained from blade coating, a trial with a perovskite of lower dimensionality, $(\text{PEA}_{0.5}, \text{BA}_{0.5})_2\text{FA}_3\text{Sn}_4\text{I}_{13}$, was attempted (table 9). The use of phenethylammonium (PEA) in combination with butylammonium (BA) has been reported to assist achieve a crystallization process with a more controlled directionality, which is what was observed during BC layer of this material even without the aid of additives. However, when the deposition was attempted by IP the results were comparable with the typical formulation, progressively increasing the printed area lowered the resolution quality and led to empty spaces in between the droplet rows.

Table 9. IP results with $(\text{PEA}_{0.5}, \text{BA}_{0.5})_2\text{FA}_3\text{Sn}_4\text{I}_{13}$ at different printing areas, ink concentration: 0.6 mol L^{-1} , WF: LV, V: 20 mV.

Conditions	Images		
DS: 55 μm Print area: 20x16 mm^2			
DS: 55 μm Print area: 40x40 mm^2			
DS: 55 μm Print area: 80x80 mm^2			

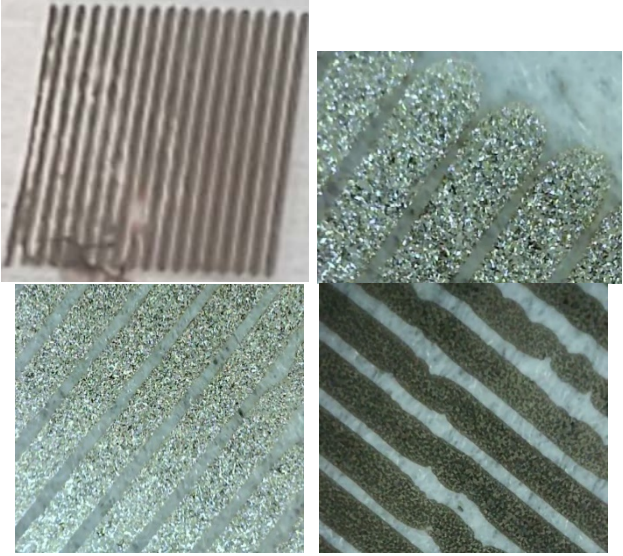
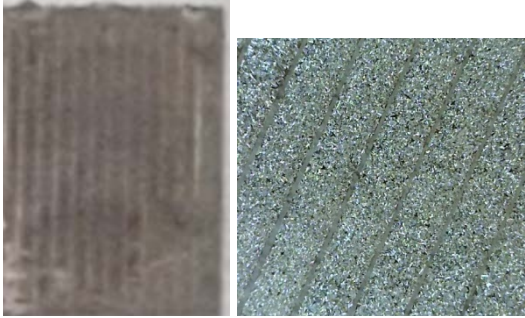
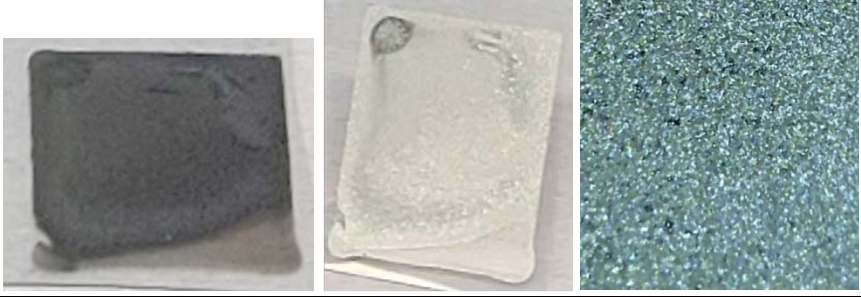
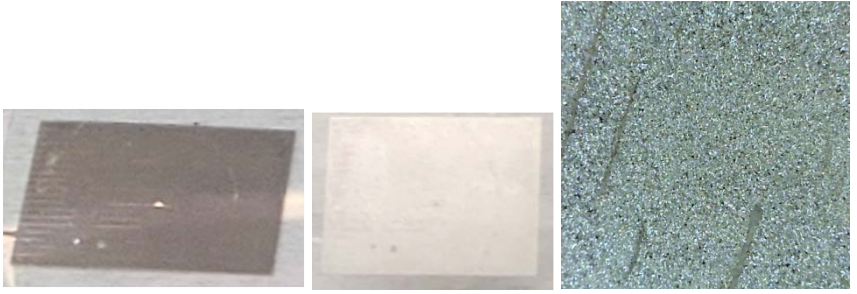
Larger prints were also attempted with the other combinations of waveforms-solvent systems (tables 10-12) optimized in D3.1; since this alternative perovskite did not seem to offer much difference regarding crystallinity, the typical formulation with DiPI and NaBH_4 was utilized for its enhanced stability. The printing with DMF:DMSO performed as expected with the WF2 waveform, the layer was relatively uniform, but the SEM image showed disconnected crystals with a lot of space in between. The GBL:DMSO ink did not work well with the WF1 or DIW waveforms, only with WF2 the coverage was improved in a narrow set of parameters, lowering the DS or increasing the potential created a heterogeneous surface; the SEM was similar to the previous case only more branched

out. In the instance of ACN:2ME on the smaller scale full layers were deposited with both DIW and WF2, once scaled the printing quality proved to be poor in comparison to the other two systems.

Table 10. Images of IP layers (small and large area) with DMF:DMSO solvent system.

Conditions	Images	
	Solvent system: DMF:DMSO (4:1)	
<p>WF: WF2 DS: 45 μm Vacuum</p>		<p>(Front) (Backside)</p>
<p>WF: WF2 DS: 45 μm Print area: 80 x 80 mm^2</p>		

Table 11. Images of IP layers (small and large area) with GBL:DMSO solvent system.

Conditions	Solvent system: GBL:DMSO		
<p>WF: WF1 DS: 45 μm V: 25 mV</p>	 <p style="text-align: center;">(Front) (Backside)</p>		
<p>WF: DIW DS: 45 μm V: 30 mV</p>			
<p>WF: WF2 DS: 20 μm V: 40 mV</p>			
<p>WF: WF2 DS: 45 μm V: 30 mV</p>			

<p>WF: WF2 DS: 45 μm V: 40 mV</p>	
<p>WF: WF2 DS: 45 μm V: 40 mV Print area: 80 x 80 mm^2</p>	

Table 12. Images of IP layers (small and large area) with ACN:2ME solvent system.

Conditions	Solvent system: ACN-2ME		
WF: DIW DS: 45 μm V: 25 mV			
WF: WF2 DS: 45 μm V: 40 mV			
WF: WF2 DS: 20 μm V: 40 mV			
WF: WF2 DS: 20 μm V: 40 mV Print area: 80 x 80 mm^2			



All three solvent systems exhibited the characteristic XRD and PL signals for FASnI_3 (figure 26), with some secondary peaks related to 2D phases. One of the more telling results was the thickness profile of the layers, which was higher than anticipated; it also showed that the coverage was indeed not complete and there were a lot of points where the HTM surface was exposed, this being the main problem that needs to be resolved when considering the operation of completed devices.

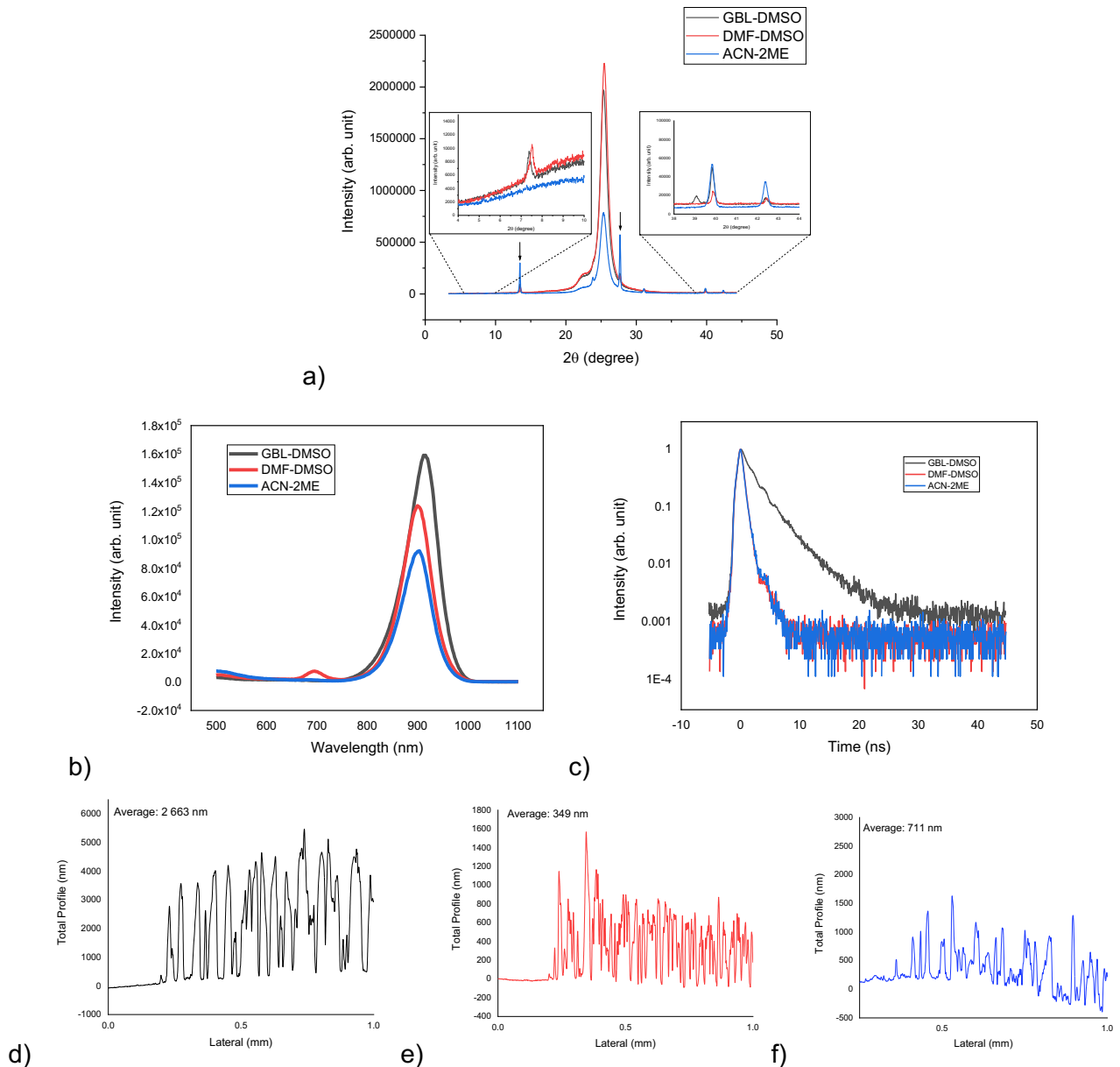


Figure 26. Characterization of IP layers a) XRD spectra b) PL spectra c) TRPL spectra, thickness profile of d) DMF:DMSO film, e) GBL:DMSO film, f) ACN:2ME film.



3.6.2 Inkjet-printed tin-based perovskite solar cells under 1 sun illumination

The tests of inkjet-printed devices only showed relevant photovoltaic results (figure 27, table 12) when the perovskite was deposited without heating the substrate, with a minor improvement when BuAc was included in the precursor; all the other batches made with the DMF:DMSO 4:1, GBL:DMSO and ACN:2ME solvent systems and the optimized jetting waveforms were unsuccessful to generate consistent working devices. Based on the previously analysed characterization of the films this is most likely caused by the poor coverage of the perovskite layer.

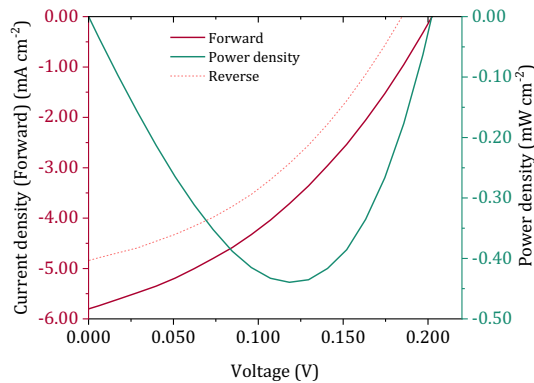


Figure 27. I-V Curve of best performance inkjet-printed cell under 1 Sun illumination.

Table 12. Average and best I-V parameters of cells under 1 Sun illumination.

Conditions			J _{sc} (mA·cm ⁻²)	V _{oc} (V)	FF (%)	PCE (%)
DMF:DMSO (9:1) + BAAC WF: LV	DS: 75 μm T: 30 °C	Average 10/12 working devices	4.55 ± 0.80	0.16 ± 0.03	35.6 ± 2.4	0.30 ± 0.10
		Best	5.7	0.20	38.9	0.44
	DS: 75 μm T: 45 °C	Average 9/12 working devices	2.45 ± 0.01	0.06 ± 0.01	30.6 ± 1.2	0.04 ± 0.01
		Best	2.60	0.07	32.2	0.06
	DS: 75 μm T: 60 °C	Average 6/6 working devices	3.77 ± 0.610	0.08 ± 0.01	31.4 ± 1.8	0.10 ± 0.03
		Best	3.68	0.10	34.1	0.13
	DS: 45 μm T: 60 °C	Average 6/6 working devices	2.08 ± 0.36	0.06 ± 0.02	31.8 ± 1.3	0.04 ± 0.02
		Best	2.28	0.08	32.5	0.06
DMF:DMSO (9:1) + BAAC + BuAc WF: LV	DS: 75 μm V: 20mV T: 30 °C	Average 12/12 working devices	3.8 ± 0.6	0.22 ± 0.05	37.5 ± 4.7	0.31 ± 0.11
		Best	3.9	0.27	44.4	0.47



DMF:DMSO (9:1) + BAAC + α -PC WF: LV	DS: 75 μ m V: 20mV T: 30 °C	Average 2/6 working devices	1.6 \pm 0.4	0.03 \pm 0.01	29.6 \pm 2.5	0.02 \pm 0.01
		Best	1.9	0.04	27.9	0.02
DMF:DMSO (4:1) + BAAC WF: WF2	DS: 45 μ m V: 40 mV T: 30 °C	*No devices out of a batch of 12 exhibited a measurable J-V curve.				
GBL:DMSO (7:3) + BAAC WF: WF2	DS: 45 μ m V: 40 mV T: 30 °C	*No devices out of a batch of 12 exhibited a measurable J-V curve.				
ACN:2ME (3:2) + BAAC WF: DIW	DS: 45 μ m V: 40 mV T: 30 °C	*No devices out of a batch of 12 exhibited a measurable J-V curve.				

4 Deviations from the workplan

As mentioned in the introductory sections the spin-coating was exploited as a benchmark of device's performance and blade-coating technique was employed as supporting method to study scalable deposition in parallel to the inkjet printing under inert atmosphere.

5 Conclusions & Future directions

Tin-based LFP solar cells were manufactured in a p-i-n structure with the Glass- or PET-ITO/PEDOT:PSS/FASnI₃/C₆₀/BCP/Ag architecture using spin-coating, blade-coating or inkjet printing as the deposition method for the absorber layer. On the one hand, an average efficiency of 9.6% \pm 0.6, (10.6% max), was obtained for the devices prepared through spin-coating of the precursor solution with the additives incorporated, DiPI and NaBH₄. It is important that as far as we know **we reported the highest stability in the literature with more than 1300 hr at 1 sun maximum power point conditions in N₂ atmosphere**, which was the center of our high level publication in Joule [8]. On the other hand, with the best conditions for blade coating an average efficiency of 2.0% was reached under 1 Sun (2.2% max), and of 5.5% in low light conditions (9.3% max), with an active area of 0.64 cm²; both the V_{OC} and J_{SC} were lower than expected, so the interface between the perovskite and charge transport layers need to be improved, in order to get closer to the goals set for this project.

Also, even though the incorporation of DiPI and NaBH₄ offered internal stability to the precursor ink and the perovskite material, the implementation of alternative ETMs and passivation methods should be continued during inkjet printing in the following stages to enhance as much as possible the intrinsic resistance of the devices to degradation mechanisms.



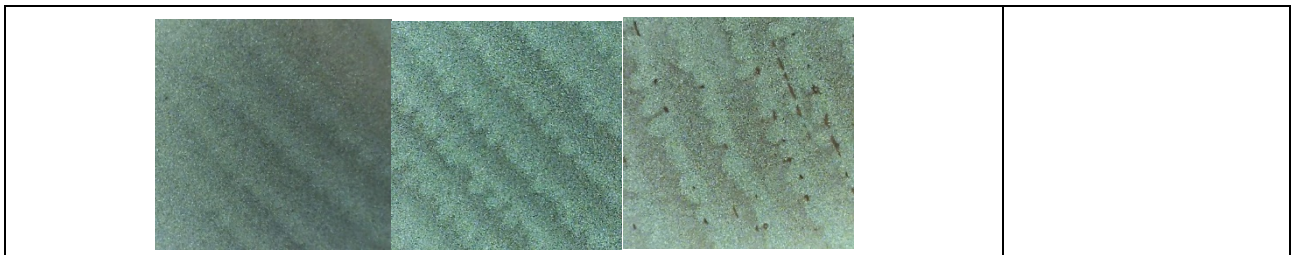
The best inkjet printed device achieved a PCE of 0.47% under standard testing conditions. Future efforts will concentrate on improving the device efficiency further by introducing a vacuum assisted annealing step to mimic the anti-solvent quenching effect.

Regarding the inkjet printed devices, although many variations of waveform parameters and printing conditions were tested, the scaling of quality layers remains as a challenge to further develop the efficiency of the devices; the main issues and possible solutions are identified in table 13 and will be addressed in future works.

Finally, it is worth to note that we will focus on different tin-based Ruddlesden-Popper phases (high-n and 2D-3D assemblies) as G-LFPs, as summarized in Table A1 (Annex 1), for future developments of our solar cells, in order to advance in efficiency and stability.

Table 13. Main issues and possible solutions of inkjet printing Sn-LFPs devices.

Identified issue		Possible solutions
<p>Balance between print coverage and perovskite crystallinity.</p>		<p>Ink engineering with different additives to improve the wettability at higher DS to ensure a better blending between the different printed rows.</p> <p>Introduction of SnCl_2 and GeI_2 to assist the crystal growth process and conceivably improve the perovskite layer interfaces.</p> <p>Implementation of a proper pre-annealing protocol, with the recently purchased VC2509A vacuum chamber.</p>
<p>Layer uniformity: thickness gradients, coffee ring effect.</p>		
<p>Layer surface: smoothness/roughness</p>		
<p>Blade coating:</p>	<p>Inkjet printing:</p>	
<p>Print area dependence</p>		



6 References

- [1] Li, Z., Klein, T. R., Kim, D. H., Yang, M., Berry, J. J., van Hest, M. F. A. M., & Zhu, K. Scalable fabrication of perovskite solar cells, *Nature Reviews Materials*, **2018**, 3, 1-20.
- [2] Bakr, Z. H., Wali, Q., Fakharuddin, A., Schmidt-Mende, L., Brown, T. M. Rajan, J. Advances in hole transport materials engineering for stable and efficient perovskite solar cells, *Nano Energy*, 2017, 34, 271-305.
- [3] W. Shockley, H. J. Queisser, *J. Appl. Phys.* **1961**, 32, 510-519.
- [4] J. Jeong, M. Kim, J. Seo, H. Lu, P. Ahlawat, A. Mishra, Y. Yang, M. A. Hope, F. T. Eickemeyer, M. Kim, Y. J. Yoon, I. W. Choi, B. P. Darwich, S. J. Choi, Y. Jo, J. H. Lee, B. Walker, S. M. Zakeeruddin, L. Emsley, U. Rothlisberger, A. Hagfeldt, D. S. Kim, M. Grätzel, J. Y. Kim, *Nature* **2021**, 592, 381-385.
- [5] B.-B. Yu, Z. Chen, Y. Zhu, Y. Wang, B. Han, G. Chen, X. Zhang, Z. Du, Z. He, *Adv. Mater.* **2021**, 33, 2102055.
- [6] M. Pitaro, E. K. Tekelenburg, S. Shao, M. A. Loi, *Adv. Mater.* **2022**, 34, 2105844.
- [7] L. He, H. Gu, X. Liu, P. Li, Y. Dang, C. Liang, L. K. Ono, Y. Qi, X. Tao, *Matter* **2020**, 2, 167-180.
- [8] J. Sanchez-Diaz, R. S. Sánchez, S. Masi, M. Krečmarová, A. O. Alvarez, E. M. Barea, J. Rodriguez-Romero, V. S. Chirvony, J. F. Sánchez-Royo, J. P. Martinez-Pastor, I. Mora-Seró, *Joule* **2022**, 6, 861-883.



7 Annex

Table A1 B-LFP/G-LFP materials/layers for solar cell applications

B-LFP	Spin-coating	Inkjet printing	Doctor blading
FASnI ₃	Yes	Yes	Yes
FASnI ₃ + additives	Yes	Yes	Yes
MASnI ₃ (FA-MA)SnI ₃ FASnI ₃	Yes	Yes	Yes
(PEA _{0.5} ,BA _{0.5}) ₂ FA ₃ Sn ₄ I ₁₃	Yes	Yes	Yes
G-LFP	Spin-coating	Inkjet printing	Doctor blading
Dip ₂ FA ₉ Sn ₁₀ I ₃₁	Yes	Yes	Yes
(PEA _{0.5} ,BA _{0.5}) ₂ FA ₉ Sn ₁₀ I ₃₁	Yes	Yes	Yes
R ₂ A _{n-1} Sn _n I _{3n+1} R= TEA, PEA, RA(Alkylammonium) A= FA	Planned	Planned	Planned